2016

Optimizing Sn-based Anode Nanostructure and Binder Material for use in High-performance Lithium-ion Batteries

Yanfei Xu
University of Wollongong, yx867@uowmail.edu.au

UNIVERSITY OF WOLLONGONG

Institute for Superconducting & Electronic Materials,

Engineering and Information Sciences

Optimizing Sn-based Anode Nanostructure and Binder Material for use in High-performance Lithium-ion Batteries

BY

YANFEI XU, B. ENG.

"A thesis submitted in fulfilment of the requirements for the award of the degree of

MASTER OF PHILOSOPHY

at the University of Wollongong"

2016

CERTIFICATION

I, Yanfei Xu, declare that this thesis, submitted in fulfilment of the requirements for the award of Master of Philosophy, in the Institute for Superconducting & Electronic Materials, Faculty of Engineering, University of Wollongong, is totally my own work unless otherwise referenced or acknowledged. This document has not been submitted for qualifications at any other academic institution.

Yanfei Xu

1 May, 2016

DEDICATION

For my beloved family and friends, who love and support me all the time

ACKNOWLEDGEMENTS

First of all, I would like to express my deepest appreciation to my research supervisor, Dr. Shulei Chou, and co-supervisors, Dr. Yunxiao Wang and Dr. David Wexler, for their rich academic knowledge, guidance, supervision, financial support of my experiments and constant encouragement during my two-years Master's study in the Institute for Superconducting and Electronic Materials (ISEM) at the University of Wollongong in Australia.

Furthermore, I would like to express my utmost appreciation to Prof. Shi-Xue Dou, Director of the Institute for Superconducting & Electronic Materials, and Prof. Hua-Kun Liu, for their constant encouragement.

As well, I would like to thank Dr. Tania Silver for her critical reading of my manuscripts and thesis. I thank all the staff members of ISEM and all the technicians in the Department of Materials Enginering for their kind assistance, including Dr. Germanas Peleckis (XRD), Dr. Kosta Konstantinov (BET, TGA/DTA), Mr. Tony Romeo (SEM, EDS), Dr Gilberto Casillas Garcia (TEM, EDS), Mrs. Crystal Mahfouz, Mrs. Narelle Badger, Mrs. Joanne George (OH&S), Mr. Robert Morgan, Mr. Mathew Davis, and Mrs. Candace Gabelish. Moreover, many thanks to Dr. Xun Xu, Dr. Yi Du, Prof. Jiazhao Wang, Dr. Jianping Yang, Dr. Weijie Li, Ms. Qiuran Yang, Mr. Boyang Ruan, Mr. Weihong Lai, and other students at ISEM, for their kind help and valuable advice.

Last, but not least, I would like to express my deep appreciation and love to my family, who have been standing behind me and encouraging me to move forward all the time, especially my lovely son Daniel and beautiful daughter Michelle who bring me so much happiness. Without their support and understanding, it would have been impossible for me to finish this thesis.

Again, please accept my sincere appreciation and best wishes to all of you.

ABSTRACT

Rechargeable lithium-ion batteries (LIBs), which are the most important electrochemical energy storage devices for small electronic devices and emerging electrical/hybrid vehicles, have been reigning over current rechargeable battery markets due to their high energy densities and great longevity. In recent years, numerous efforts have been made to develop new electrode materials to meet the demand for batteries with higher energy density and enhanced cycling stability. For anode materials, Tin (Sn) serves as a promising alternative to conventional carbonaceous anode active materials due to its ability to react with more lithium ions and achieve higher capacity based on the alloying/de-alloying mechanism. My Master's work toward the commercialization of Sn anode has been focused on the systematic investigation on this anode material, including the fabrication of ultrafine Sn nanoparticles, exploration of a novel binder, and developing a superior nanostructured configuration of the active material.

Ultrafine Sn nanoparticles have been fabricated via a facile reduction reaction at room temperature with the aid of ultrasonication. When applied as a potential anode in LIBs, various polymer binders were utilized and investigated, including polyvinylidene fluoride (PVDF), carboxymethyl cellulose (CMC), and epoxy resin (Part A) – amine (Part B) glue (AB). Surprisingly, the obtained electrode (denoted as Sn-AB) realizes the homogeneous dispersion of Sn active nanoparticles in AB binders via forming coordination complexes around the oxidized surfaces of Sn nanoparticles during the curing process for Part A and Part B. The electrode exhibits a stable capacity of ~ 400 mA h g^{-1} over 100 cycles and superior rate capability for fast charge/discharge processes (~ 235 mA h g^{-1} at 5 A g^{-1} in comparison to ~ 475 mA h g^{-1} at 0.2 A g^{-1}). This is the best performance of pure Sn nanoparticles with various binders ever reported so far.

An elaborate core-shell nanostructure has been designed and prepared via simultaneous reduction of ultrafine SnO_2 nanoparticles and carbonization of oleic acid (OA) ligands via a facile low-temperature heat treatment (500 °C). Sn@SnO_2 grafted graphene nanocomposite (Sn@SnO_2/G) was successfully fabricated. The

strategy developed herein offers an ingenious method to prepare unique $Sn@SnO_2/G$ via a one-step heat-treatment. Moreover, it also can be used to prepare green graphene nanosheets via etching away the interior $Sn@SnO_2$. When applied as anodes in LIBs, the obtained $Sn@SnO_2/G$ impressively delivers a sustainable capacity of ~ 600 mA h g^{-1} over 100 cycles. In comparison with SnO_2/reduced graphene oxide (RGO), the $Sn@SnO_2/G$ electrode exhibits much better rate capability. At a medium current rate (500 mA g^{-1}), the $Sn@SnO_2/G$ and SnO_2/RGO deliver comparable reversible capacity of 470 and 422 mA h g^{-1} over 15 cycles, respectively, but the $Sn@SnO_2/G$ is capable of achieving a much higher capacity of 167 mA h g^{-1} at the very high rate of 5 A g^{-1}.

TABLE OF CONTENTS

LIST OF FIGURES

LIST OF TABLES

LIST OF SCHEMATICS

CHAPTER 1 INTRODUCTION

1.1 General background

Lithium-ion batteries are attracting tremendous attention in scientific and industrial fields due to their high electromotive force, high energy density, and reasonable cycle life. LIBs serve as the main power source for portable electronic devices in our daily lives, including cellular phones and laptops. LIBs are now expected to hold great promise for emerging electric vehicles. In order to meet the requirements of such high energy density devices on a large scale, the development of high-capacity electrode materials for LIBs has been the focus of research throughout the world. Among the anode candidates, metallic tin (Sn) has been regarded as one of the most promising alternatives to conventional graphite (LiC_6, 372 mA h g^{-1}) based on the following reasons. Firstly, the Sn anode possesses high theoretical capacity ($Li_{4.4}Sn$, 992 mA h g^{-1}). Secondly, the charge/discharge platform of Sn is higher than that of graphite, so that the batteries with Sn anode are much safer. Moreover, Sn does not experience solvent intercalation, thereby avoiding irreversible charge losses. Unfortunately, the practical application of tin active anode is hindered by the huge volume expansion during the lithiation/de-lithiation processes, which result in pulverization of the active materials, serious cracks on the electrode surface, and rapid capacity decay. A tin electrode without an appropriately designed structure would fail after only a few charge/discharge cycles.

This Master's work has the aim of developing and optimizing Sn-based electrode materials for practical application. The research effort is devoted to explore a novel binder for pure Sn nanoparticle, which could confine the Sn nanoparticles in place with high resistance to strain, serving as tensile networks to significantly alleviate the huge stress of Sn nanoparticles during the lithiation/delithiation process. On the other hand, the strategy of nanostructuring Sn-based nanocomposite is applied to achieve enhanced electrochemical properties for use in rechargeable lithium-ion batteries. Specifically, the key points of this thesis are outlined as follows: a) Choosing simple and scalable synthesis methods for commercialization, including the room-temperature precipitation method and the high-temperature calcination method. b)

Enhancing the Li-storage capacity via fabricating nanosized Sn particles. c) Constructing special nanostructures via the incorporation of the active material (Sn) into a conductive matrix (graphene). d) Optimizing the electrode integrity by developing a novel binder.

1.2 Chapter overview

Chapter 2 presents a literature review related to rechargeable lithium-ion batteries. The chapter includes an overview of the general background, a brief history, basic concepts and principles, and the general components of rechargeable lithium-ion batteries, followed by recent research and development in this area.

Chapter 3 presents the experimental and characterization methods used during the experiments in this thesis, including the details of chemicals, synthesis procedures, physical characterization techniques, and electrochemical characterization methods.

Chapter 4 presents a synthesis and characterization study of ultrafine Sn nanoparticles prepared by a simple one-step reduction reaction for application in rechargeable lithium-ion battery anodes. The as-prepared materials were investigated by X-ray diffraction (XRD), scanning electron microscopy (SEM), and transmission electron microscopy (TEM). A new type of binder, commercial epoxy resin (Part A) – amine (Part B) glue was developed as an effective binder and was utilized to prepare Sn electrode for comparison with the conventional poly(vinylidene) fluoride (PVDF) and carboxymethyl cellulose (CMC) binder. The cohesive forces of all binders were estimated via static uniaxial tensile testing on an INSTRON 5943. Coin-type half-cells were assembled, and their electrochemical properties were investigated by using cyclic voltammograms and galvanostatic charge/discharge cycling.

Chapter 5 continues with carbon coating as an approach to improving the electrochemical properties of Sn anodes used in rechargeable lithium-ion battery anode. In this chapter, a core-shell $Sn@SnO_2$ grafted graphene nanocomposite ($Sn@SnO_2/G$) was successfully fabricated by simultaneous reduction of ultrafine

SnO_2 nanoparticles and carbonization of oleic acid (OA) ligands via a facile low-temperature heat treatment (500 °C). The morphologies of the powders were investigated by field-emission scanning electron microscopy (FESEM) and transmission electron microscopy (TEM). The Brunauer-Emmett-Teller (BET) method was utilized to calculate specific surface areas (S_{BET}). The surface morphology and thickness of the graphene nanosheets were examined by atomic force microscopy (AFM Asylum Research MFP-3D) at room temperature. The electrochemical tests were conducted by assembling coin-type half-cells in an argon-filled glove box. The electrochemical performance was tested on a LAND Battery Tester. Cyclic voltammetry and impedance testing was performed using a Biologic VMP-3 electrochemical workstation.

General conclusions from these studies are summarized in Chapter 6.

CHAPTER 2 LITERATURE REVIEW

2.1 Introduction of rechargeable lithium-ion batteries

2.1.1 General introduction

The market for alternative vehicles, such as electric vehicles and plug-in hybrid electric vehicles, has quickly grown and become very important. The electric vehicle (EV) revolution not only enables us to reduce the usage of petrol for transportation, but also satisfies the environmental constraints. Nevertheless, the development of advanced power sources for this system is still obstructed by some serious challenges and lagging far behind. Rechargeable batteries, which can store sustainable energy with long-term stability and long-term cycle life, are the critical challenge for their electrochemistry. [1]

Among these numerous energy storage technologies, rechargeable lithium ion batteries (LIBs) feature high energy density and long cycle life, which makes them potential candidates for pushing forward the electrical vehicle revolution.[2, 3] As shown in Figure 2.1a, the EVs can be categorized as hybrid EVs (HEVs), plug-in hybrid EVs (PHEVs), and full EVs, which require different levels of pure electrical propulsion and different battery-pack sizes.[1] A comparison of various battery technologies with regards to their volumetric and gravimetric energy density is shown in Figure 2.1b.[4] It can be seen that nickel metal hydride (Ni-MH) batteries with low energy density were used in hybrid EVs, which could be ascribed to their advantages of high rates, long cycle life, and excellent safety features.[5] In contrast, high-energy LIBs are being developed as power sources for EVs, which are expected to free transportation from its dependence on petrol in the medium-term future. The new generation of rechargeable LIBs should be rationally designed not only for consumer electronics, but also for clean energy storage and power supplies for EVs. In response to these requirements, developing lithium ion batteries with high- energy, low- cost, and environmental- friendliness is an urgent task, although it requires a breakthrough on materials design.

a

Modes of operation	battery capacity needed, kWh	Energy density, Wh/kg	Weight of battery, Kg	Speed, kilometres per hour	Distance on one charge, kilometres
 Hybrid	<3	40-50 (Ni-MH)	60 (Ni-MH)	100+	15
 Plug in Hybrid	5.6-18	90-100 (Li-ion)	60-200 (Li-ion)	100+	10-60
 Full EV	35-54	90-100 (Li-ion)	450 (Li-ion)	>100	150-200

b

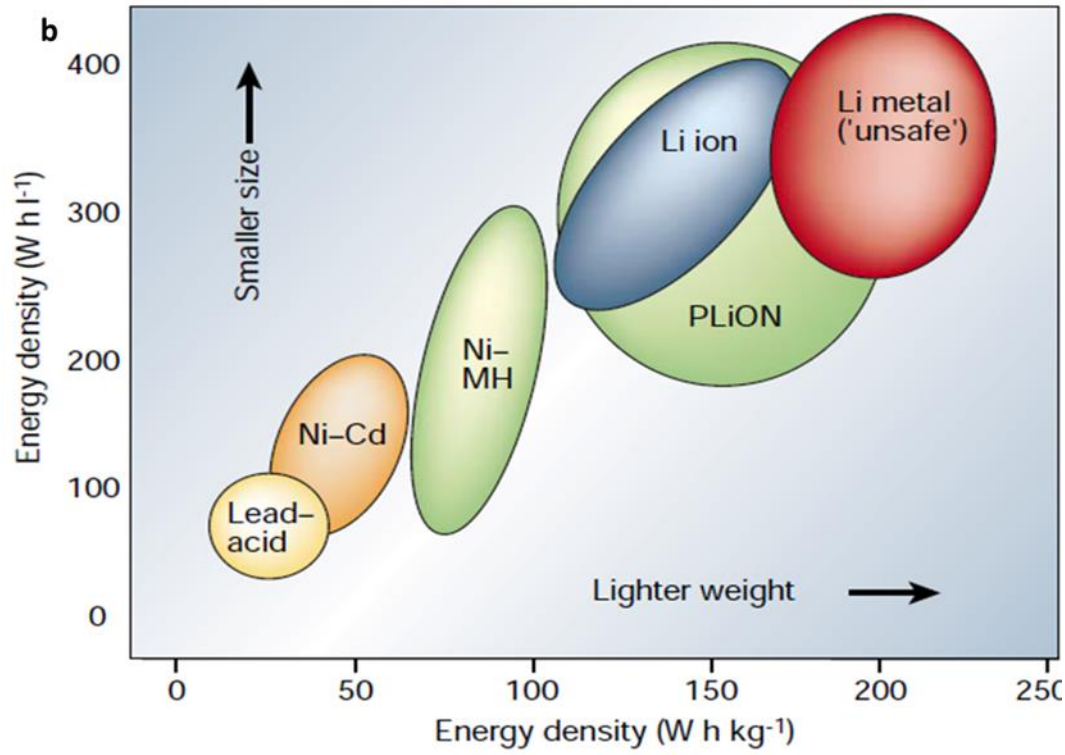

Figure 2.1 (a) Performance and battery parameters of the main three kinds of electric vehicle: hybrid, PHEV and full EV.[1] (b) Volumetric versus gravimetric energy density of different battery technologies.[4]

2.1.2 A brief history

In the 1790s, the first development of batteries was successfully demonstrated by using Li metal in the primary cells.[6] By 1972, with the finding that numerous inorganic compounds reversible react with alkali metals, electrochemical intercalation was defined, and the potential use of intercalation compounds was clearly identified.[7] In 1972, Exxon constructed a battery system with TiS_2 as cathode and Li metal as anode. This battery, however, was not viable as fabricated due to the growth of lithium dendrites, leading to an explosion hazard.[8] During the 1980s, Goodenough proposed the replacement of metallic Li with Li_xMO_2 (M = Co, Ni, or Mn), which can well address the safety issues and is still used in today's batteries system.[9] At the end of the 1980s and the early 1990s, the concept of the so-called Li-ion or rocking-chair technology was first introduced by Murphy et al.[10] and then by Scrosati et al.[11] Finally, in June 1991, the commercialization of rechargeable lithium-ion batteries based on $C/LiCoO_2$ was realized by the Sony Corporation in Japan.[12] This type of Li-ion battery, which is still popular in today's portable electronic devices, has a potential over 3.6 V and gravimetric energy densities as high as 120-150 Wh kg^{-1}. In the typical structure, a lithium ion battery consists of a graphite anode, a cathode based on $LiCoO_2$ and an electrolyte which is a lithium salt (e.g. $LiPF_6$) dissolved in a mixed organic solvent. The success of this system was based on using a layered carbon material (graphite) instead of Li metal as anode. The insertion materials act as active materials, allowing Li ions to reversibly insert and de-insert themselves leading to the transfer of Li-ions between positive and negative poles during cycling. The electrochemical processes of a typical Li-ion battery are shown in Figure 2.2. Until now, the most commonly used anode material has been graphite, and transition metal oxide and phosphate compounds, such as $LiCoO_2$, $LiMn_2O_4$, and $LiFePO_4$, are normally selected as the cathode materials.

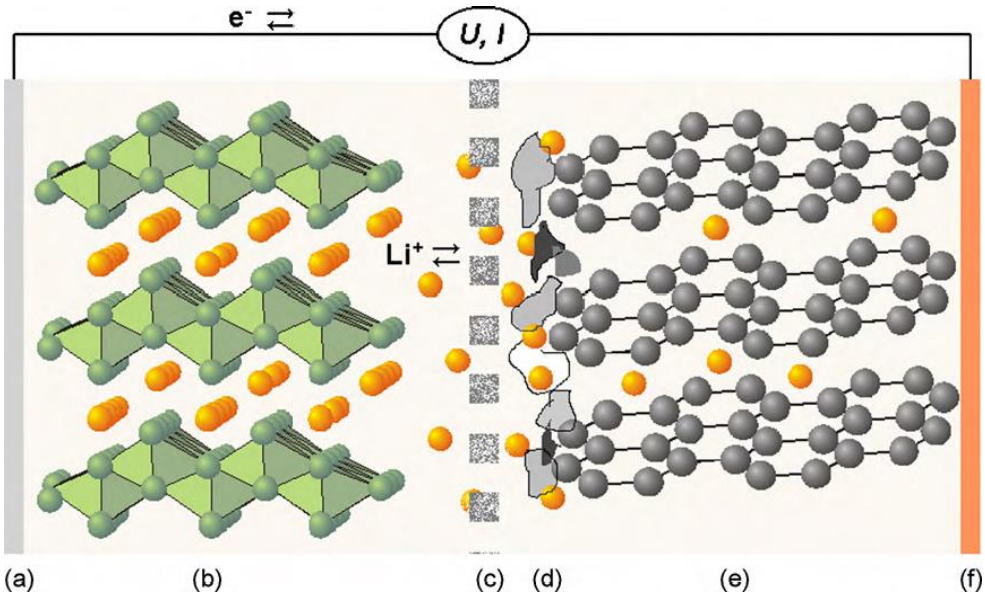

Figure 2.2 Schematic illustration of a typical Li-ion battery: (a) aluminium current collector; (b) transition metal oxide active cathode material; (c) porous separator immersed in liquid electrolyte; (d) solid electrolyte interphase (SEI) layer formed during cycling; (e) graphite active anode material and (f) copper current collector.[13]

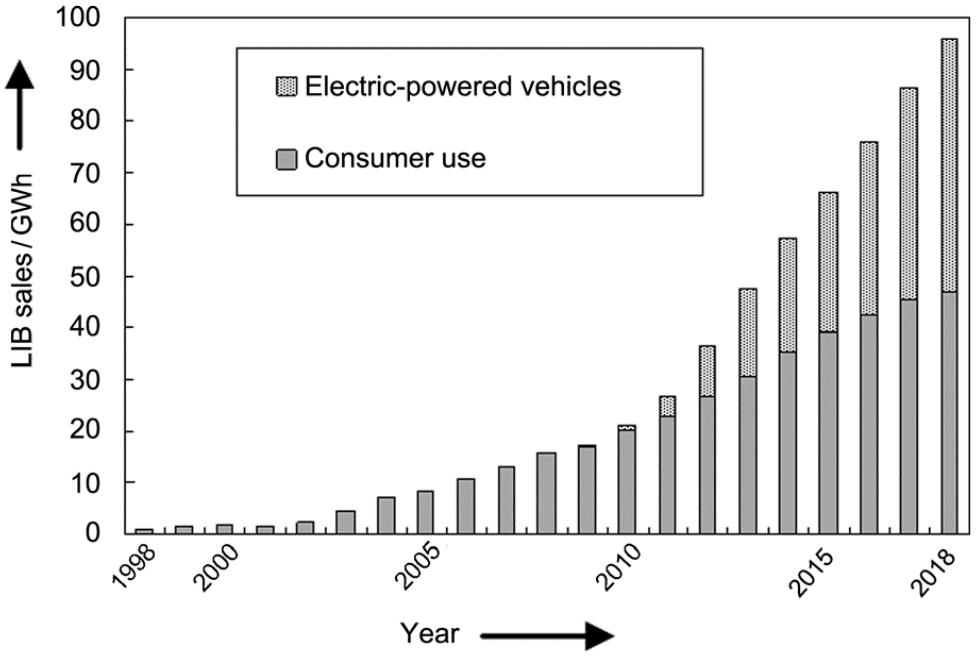

Figure 2.3 Forecast expansion in demand for lithium-ion batteries in the future. GWh = gigawatt hours.[14]

As indicated in Figure 2.3, the usage of lithium-ion batteries quite rapidly caught on and has been continuously increasing in the following years. The "consumer use" applications include portable devices such as cameras, laptop computers, mobile phones, and a variety of other electronic products. As potential power sources for electric-powered vehicles, their applications in this environmental friendly mode of transportation are forecasted to grow rapidly as well. Therefore, researchers are encouraged to focus their efforts on high-performance lithium ion batteries. The ideal combination of electrode-electrolyte-electrode could be deteremined out by selective mixing of existing and newly designed materials as negative and positive electrodes with the optimal electrolyte and binder.

2.2 Materials for the cathode

Cathode materials are among the most vital components in the LIB system, which determine the overall reversible capacity of LIBs. Since 1980, many cathode materials have been explored and reported, including $LiCoO_2$, $LiMn_2O_4$, $LiMnPO_4$, $LiFePO_4$, $Li_3V_2(PO_4)_3$, $LiVPO_4F$, and $LiVOPO_4$. As shown in Figure 2.4, the intercalation cathodes can be divided into four types according to their crystal structure: layered metal oxides, spinel oxides, olivines, and tavorites.

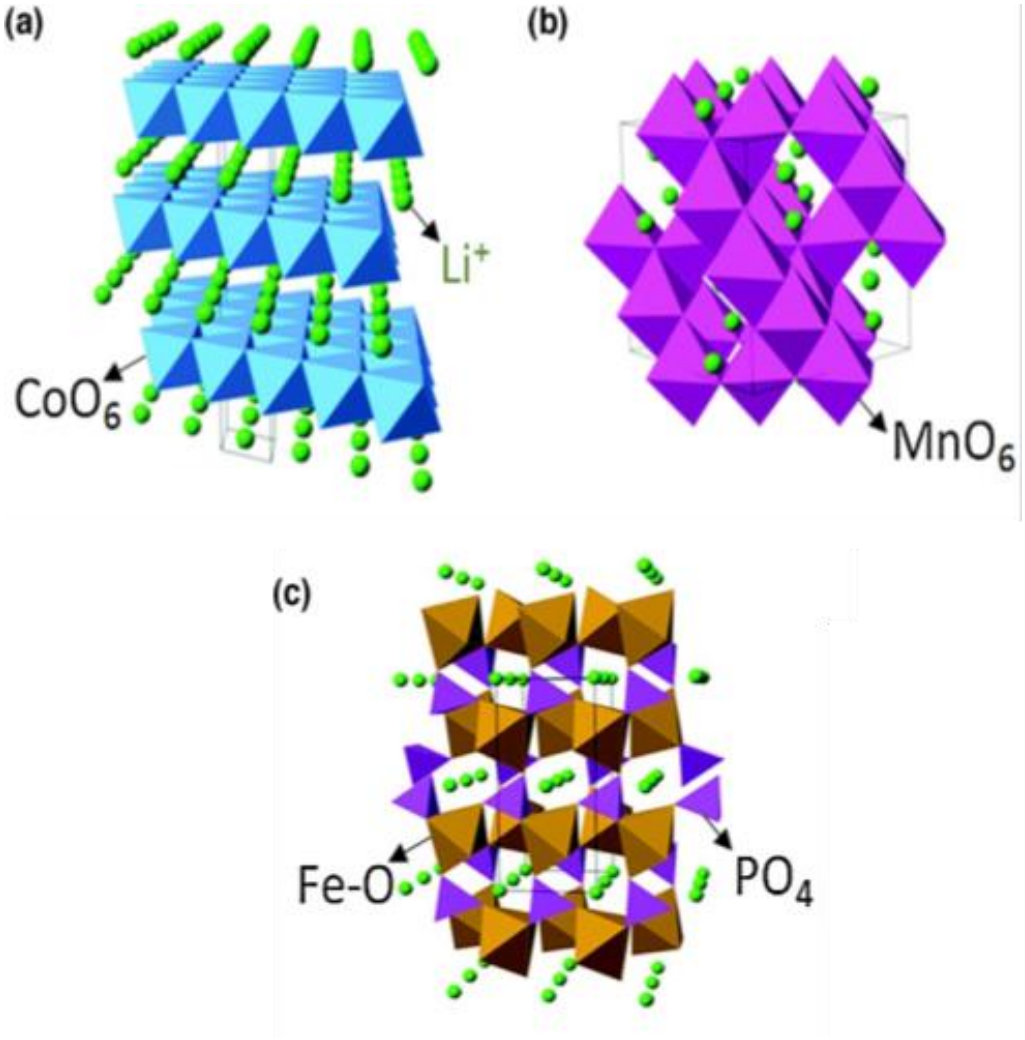

Figure 2.4 Crystalline structures and discharge profiles of representative intercalation cathodes: (a) layered $LiCoO_2$, (b) spinel ($LiMn_2O_4$), (c) olivine ($LiFePO_4$).[15]

2.2.1 Transition mental oxides

$LiCoO_2$ (LCO) is the most successful showpiece material for layered transition metal cathodes, which is still used nowadays in the majority of commercially available LIBs. As presented in the Figure 2.4a, a hexagonal symmetry is formed by the Co and Li atoms, which are located in octahedral sites and occupy alternating layers. LCO has a high theoretical specific capacity of 274 mA h g^{-1}, and a large theoretical volumetric capacity of 1363 mA h cm^{-3}. Moreover, it exhibits low self-discharge, a high discharge voltage, and good cycling stability, ensuring the successful commercialization of LCO.[15, 16]

The main limitations of $LiCoO_2$, however, are the expensive cost, fast capacity decay at high rates or during deep cycling, and poor safety record, which make it unsuitable for large-scale energy-storage applications in EVs/HEVs.[17] Therefore, various alternative cathode materials have been developed within the last two decades.

$LiNiO_2$ (LNO), possessing the same crystal structure as $LiCoO_2$, has been proposed as an alternative cathode material.[18] LNO has attracted much research enthusiasms due to its advantages in term of high theoretical capacity (275 mA h g^{-1}) and lower cost. Practical application of LNO is still restricted, however, mainly because the Ni^{2+} ions tend to substitute onto Li^+ sites during the synthetic and delithiation processes, which makes it difficult to obtain an appropriate composition for optimum lithiation/delithiation[19] and obstructs the Li diffusion pathways in the subsequent cycles.[20] After doping Co into LNO, the resultant $LiNi_{1-x}Co_xO_2$ ($x \approx 0.8$) could take advantage of the low cost and high capacity of nickel relative to cobalt.[21-23] On the other hand, the safety issue, which is probably associated with the structural changes and evolution of O_2 during the charge process, limits the commercialization of LNO.[24] Ni^{3+} substitution by Co^{3+} is a good approach to ensure the stability of the oxidation state and reduce the formation of Ni^{4+}.[25] Moreover, Mg incorporation is also favourable for improving the insufficient thermal stability at high state-of-charge (SOC), and Al or other anions doped with F^- and S^{2-} on O^{2-} sites can enhance both the thermal stability and the cycling performance.[26, 27]

$LiMnO_2$ (LMO) is another promising candidate because Mn is much cheaper and less toxic than Co or Ni. The cycling performance of LMO, however, is not adequate due to the following reasons: (1) The layered structure is prone to transfermation into spinel during the Li-ion extraction process.[28] (2) Mn dissolution occurs when a disproportionation reaction of Mn^{3+} is generated to form Mn^{2+} and Mn^{4+}, and this process is always observed for all Mn-containing cathodes.[29] The poor cycling stability, therefore, is restricting the widespread commercialization of LMO. Further research efforts have been made to explore less expensive and more stable $LiNi_xCo_yMn_zO_2$ (NMC) composites, achieving higher practical specific capacity than LCO and similar operating voltage, as well as reducing of the Co content and achieving a lower cost.[30] $Li(Ni_{1/3}Mn_{1/3}Co_{1/3})O_2$ is the most frequently-reported NMC,

which contains equal amounts of the three transition materials and has high capacity and good rate capability, as well as tolerating high voltages.[31-33]

2.2.2 Spinel oxides

The spinel $LiMn_2O_4$ is a promising alternative cathode material because of its low cost and non-toxicity compared with commercially available $LiCoO_2$. In the cubic spinel structure (shown in Figure 2.4b), Mn occupies the octahedral 16d sites, and Li is predominantly located in the tetrahedral 8a sites. Therefore, excess metal cations exist in every layer to provide a sufficiently high binding energy and preserve an ideal cubic close-packed (ccp) oxygen array, even when Li ions are extracted from the framework. The spinel $LiMn_2O_4$ offers a 3-dimensional (3D) network of channels for Li-ion diffusion, and hence realizes excellent safety and high power capability. Spinel $LiMn_2O_4$ suffers from critical defects, however, including low capacity (110 - 120 mA h g^{-1}) and low chemical stability, especially at elevated temperatures. Another challenge for spinel $LiMn_2O_4$ is the phase transformation that occurs during the cycling process.[34, 35] Also, there is obvious capacity loss caused by the irreversible side reactions with the electrolyte, and oxygen loss from the delithiation of $Li_2Mn_2O_4$ at the surface.[36, 37] Various nanostructured or single-crystalline $Li_2Mn_2O_4$ composites have shown the enhancement of the kinetics of phase transformation and minimized undesirable consequences, however, thus enabling improved of cycling performance.[38-41] For a typical example, single-crystalline $LiMn_2O_4$ nanotubes rendered superior cycling stability and high-rate capability, delivering capacity retention of 70% over 1500 cycles at the current density of 5 C.[42] Moreover, a Li-rich $Li_{1.12}Mn_{1.88}O_4$ spinel with ordered mesoporous structure was demonstrated to possess better electrochemical performance than the bulk spinel.[43]

2.2.3 Olivine

At present, lithium iron phosphate ($LiFePO_4$, LFP) batteries have been adopted as the power source in some electrical vehicles. This is because LFP is an attractive cathode material with potentially low-cost, plentiful elements, and environmentally benignity. As shown in Figure 2.4c, LFP has the olivine structure, where the Li^+ and Fe^{2+} ions are situated in octahedral sites, and the P is located in the tetrahedral positions with a

slightly distorted hexagonal close-packed (HCP) oxygen array. Each FeO_6 octahedron is connected with four FeO_6 octahedra through common corners in the *b*-*c* plane, thus forming zigzag planes. The LiO_6 octahedra form edge-sharing chains along the *b*-axis. These mean that one FeO_6 octahedron has common edges with two LiO_6 octahedra, and the PO_4 groups share one and two edges with the FeO_6 octahedron and LiO_6 octahedra, respectively.[44] Strong P-O covalent bonds in the $(PO_4)^{3-}$ polyanion not only stabilize the oxygen when fully charged, but also avoid O_2 release at high states of charge, making $LiFePO_4$ an excellent, stable, and safe cathode material. The advantages of LFP include thermal stability and high power capability. However, its major weaknesses are its relatively low potential plateau (3.4 V vs. Li^+/Li), slow ionic diffusivity (10^{-14} to 10^{-16} cm^2 s^{-1}) and poor electronic conductivity (~10^{-9} S cm^{-1} at room temperature),[45, 46] which is much lower than those of $LiCoO_2$ (~10^{-3} S cm^{-1}) and $LiMn_2O_4$ (2×10^{-5} to 5×10^{-5} S cm^{-1}).[47] Therefore, significant efforts have been made to improve the electrochemical performance of LFP. An effective strategy for improving the kinetics is the fabrication of nanosized materials.[45, 47] Generally speaking, reducing the particle size can guarantee a shorter diffusion path and a larger electrolyte/electrode contact area for the fast Li insertion and extraction reactions compared with micron-sized particles.[48-50] On the other hand, conductive surface coatings, such as with C, Cu, Ag, graphene, and conducting polymers, are able to increase the conductivity of materials, and improve their cycling performance.[51, 52] Furthermore, incorporation of LFP with supervalent cations or anion doping (e.g. F^{-1}, Cl^{-1}) is also an effective approach for improving the bulk conductivity by eight orders of magnitude.[53, 54]

$LiMnPO_4$ (LMP), as another olivine structural material, has a higher voltage of 4.1 V vs. Li/Li^+. The kinetics of LMP, however, is unusually sluggish, possibly due to the intrinsically low ionic and electronic conductivity, and the huge interfacial strain between the lithiated and delithiated phases.[55] Also, Jahn-Teller distortion is triggered by the heavy polaronic holes located on the Mn^{3+} sites in delithiated $MnPO_4$ and the large volumetric changes during the charge-discharge process from $LiMnPO_4$ to $MnPO_4$, which combine together to hinder the application of $LiMnPO_4$. Similarly, the reduction of particle size and coating with conductive materials are

supposed to be the promising methods for $LiMnPO_4$.[56-58]

2.3 Materials for the anode

Anode materials are necessary in Li-ion batteries for pairing with the above-discussed cathode electrodes. Li metal as an anode material is not feasible and unsafe, because it results in the formation of Li dendrites, short-circuiting and a thermal run away reaction on the cathode, setting the battery on fire. In addition, Li metal also suffers from poor cycle life. Generally, anode materials for LIBs can be classified into three main categories based on the reaction mechanism with Li: intercalation, alloying, and conversion (displacement) types (Figure 2.5)

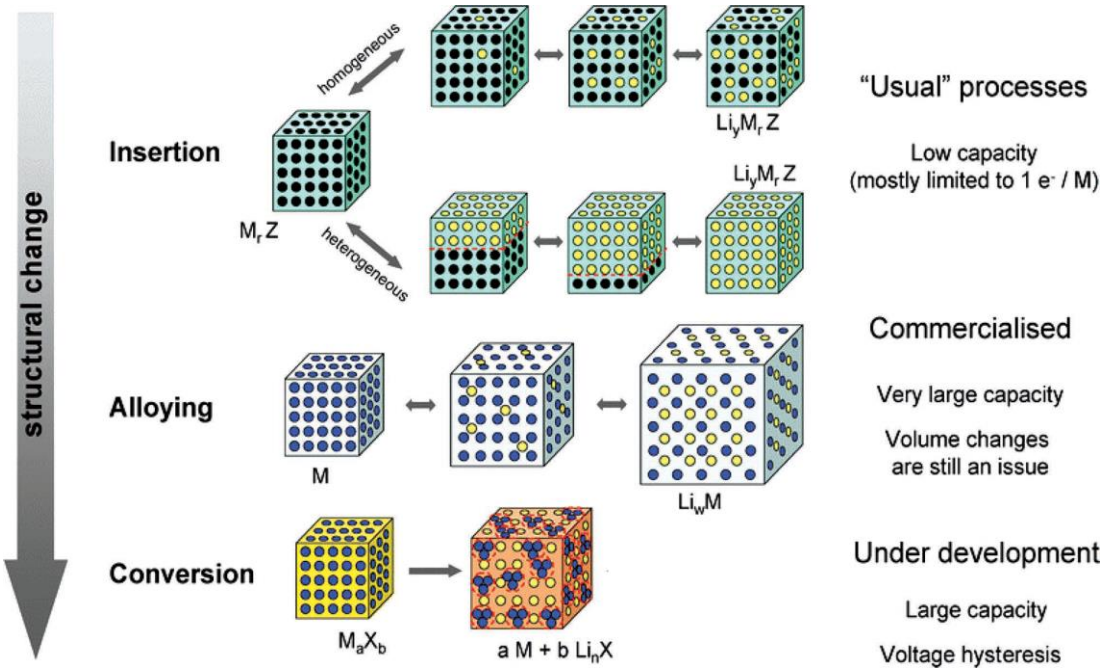

Figure 2.5 Schematic representation of the different reaction mechanisms in electrode anode materials for lithium-ion batteries. Black circles: voids in the crystalline structure, blue circles: metal atoms, and yellow circles: lithium ions.[59]

2.3.1 Intercalation materials

Carbon has been the commercially available anode material for the Li-ion battery for more than 20 years, and it is still the preferred choice of anode material. The electrochemical activity of the carbon anode material comes from the intercalation of

Li between the graphene planes, which provide the good 2D mechanical stability, high electrical conductivity, and fast Li transport. One Li atom can react with and store six C atoms in this approach. Carbon features the combined properties of low cost, abundant availability, low delithiation potential vs Li, fast Li diffusivity, high electrical conductivity, and negligible volume changes during lithiation/ delithiation processes. Furthermore, carbon has an attractive balance of cycling stability, and moderate energy and power density compared to other intercalation-type anode materials. At present, there are three main types of carbon anodes used in lithium-ion batteries, including soft carbon, hard carbon, and graphite (Figure 2.6). Since 1990, a great many efforts have been made to replace graphite anode with high capacity anode materials. For this purpose, non-graphitized carbon materials, such as soft and hard carbon, have been widely studied.[60, 61]

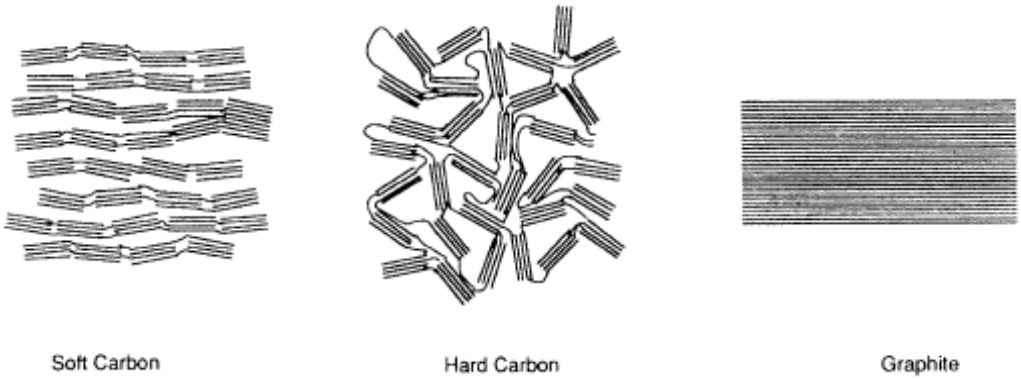

Figure 2.6 Typical structures of three different kinds of carbonaceous materials used as anodes for LIBs.[60]

2.3.2 Alloy materials

Li-alloying materials including semi-metallic and metallic materials, as well as various compounds, have been investigated during the past few decades. Among these various Li alloy materials, silicon and tin-based composites have been developed as typical anodes for LIBs, which render far greater volumetric and specific capacities than graphite. As displayed in Figure 2.7, Si and Sn have superior theoretical specific capacities (4200 and 993 mA h g^{-1}, respectively). Unfortunately, huge volume changes could be occurred during the electrochemical cycling

processes for Sn (~300 %) and Si (~400 %), respectively.[62, 63]

Si has been considered as a very promising anode material for Li-ion batteries, due to its having the highest gravimetric and volumetric capacity (4200 mA h g^{-1}), as well as natural abundance (26.4 %), and environmental friendliness.[62] Si anode, however, suffers from intrinsically low electronic conductivity (2.52×10 -4 /(m.Ω)), large volume expansion (~ 400 %), and an unstable solid interphase SEI film during the discharge/charge reactions, which leads to very fast capacity fading and inferior cycling life.

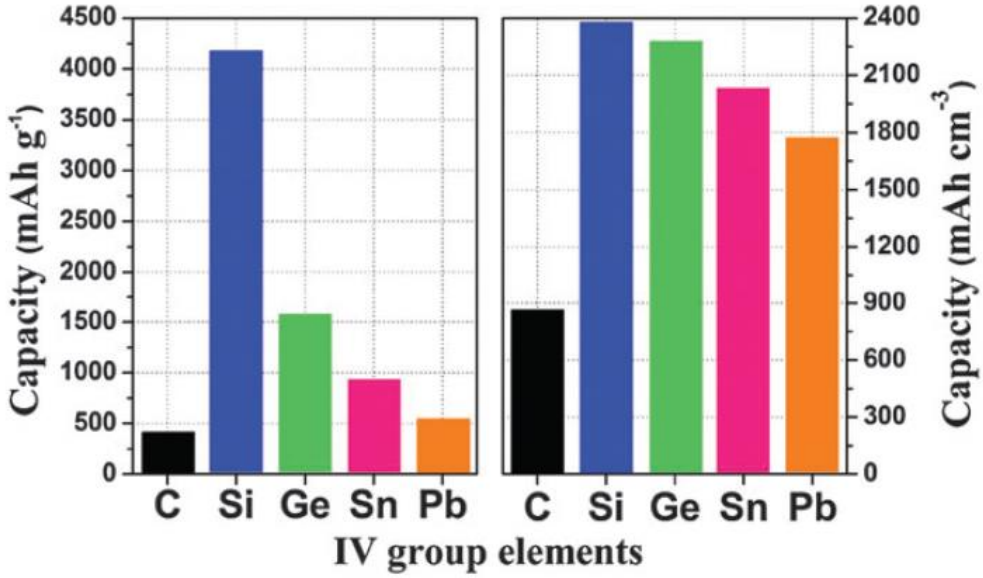

Figure 2.7 Gravimetric (left) and volumetric (right) capacities of C (LiC_6), Si ($Li_{4.4}Si$), Ge ($Li_{4.25}Ge$), Sn ($Li_{4.25}Sn$), and Pb ($Li_{4.25}Pb$) anodes.[64]

To address these problems, incorporation with a conductive substrate or constructing unique Si nanostructures have been demonstrated to be the most effective strategies.[65-68] For instance, a unique silicon-carbon yolk-shell nanostructure has been reported, in which the carbon shell could improve the electrical conductivity of the electrode, and the free space could sufficiently accommodate volume expansion and endure larger stresses (Figure 2.8).[69] For preparing such yolk-shell structures, commercial Si nanoparticles were first encapsulated by a dense coating of SiO_2 as the middle layer and then by polydopamine as the outer layer; after carbonization

under nitrogen atmosphere and selected removal of SiO_2 by hydrofluoric acid, Si@void@carbon composites were obtained. Although Si-based anodes have demonstrated very promising performance with the aid of various nanostructures (i.e., nanowires, nanotubes, and 3D porous particles), their complex synthetic processes, as well as their low capacity retention, have seriously hindered the practical application of Si.

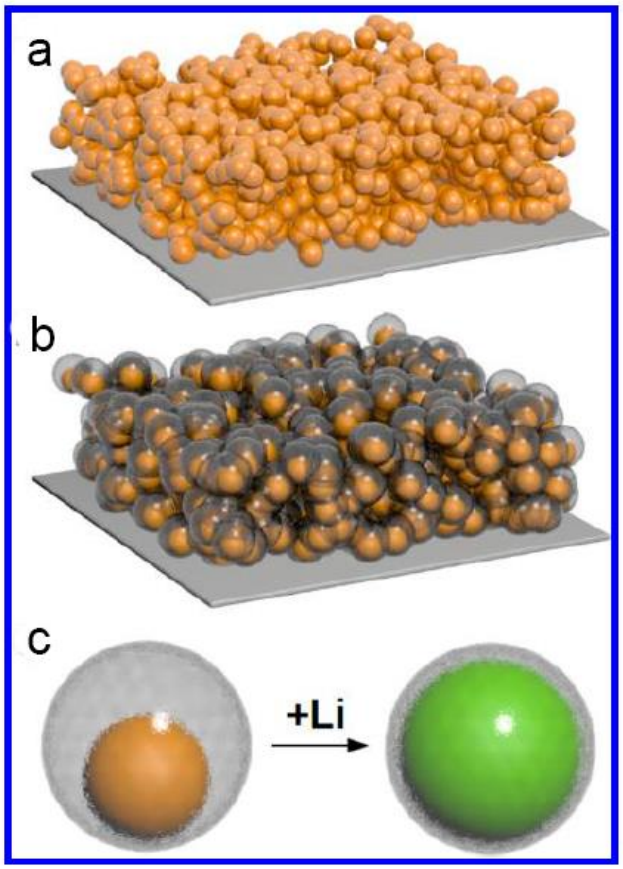

Figure 2.8 Schematic illustration of the materials design for (a) a conventional Si nanoparticle electrode, (b) a novel Si@void@C yolk-shell electrode; (c) a magnified schematic illustration of an individual Si@void@C yolk-shell nanoparticle indicating that the void space is large enough to accommodate the expansion of the Si NP without breaking the carbon coating layer or disrupting the SEI film on the outer surface.[69]

2.3.3 Conversion materials

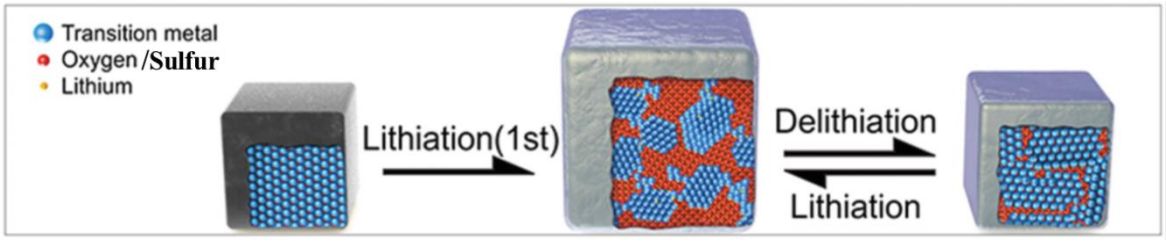

Figure 2.9 Schematic representation showing the discharge-charge process mechanisms for conversion reactions.[70]

Various metal oxides and sulfides have been extensively proposed as the high-capacity anode materials for LIBs. As described in Figure 2.11, the reaction mechanism of transition-metal oxides and sulfides (MX, where M = Fe, Co, Cu, Ni, etc; X=O, S) are obviously different from the Li-intercalation and Li-alloying processes, which involve the formation of metal and Li_2X nanograins. This type of reaction mechanism undergoes little volume change and features high reversibility, leading to superior capacity and decent cycling stability. Nevertheless, this reaction causes low initial Coulombic efficiency, unstable SEI film formation, large potential hysteresis, and unsatisfactory capacity retention. To settle these issues, research work has been mainly focused on the fabrication of nanostructured architectures and the introduction of conductivity carbon.[71-80]

Magnetite (Fe_3O_4) is a very attractive anode material because of its the great advantages, including high abundance, low cost, less toxicity, and large theoretical capacity, as well as superior resistance to corrosion. Studies have been devoted to structural control with the elaborate hierarchical morphology. Recently, Lee et al. reported a C-coated hierarchical nanostructure, which featured a spherical sea-urchin-like shape 200-500 nm in diameter (Figure 2.12b). The as-designed nanoparticles were composed of the inner Fe_3O_4 cores and outer carbon shells. (Figure 2.12c). Unlike the traditional Fe_3O_4 nanoparticles with obvious capacity decay, the capacity of the C-Fe_3O_4 nanocomposite increased slowly as cycling was prolonged times and eventually

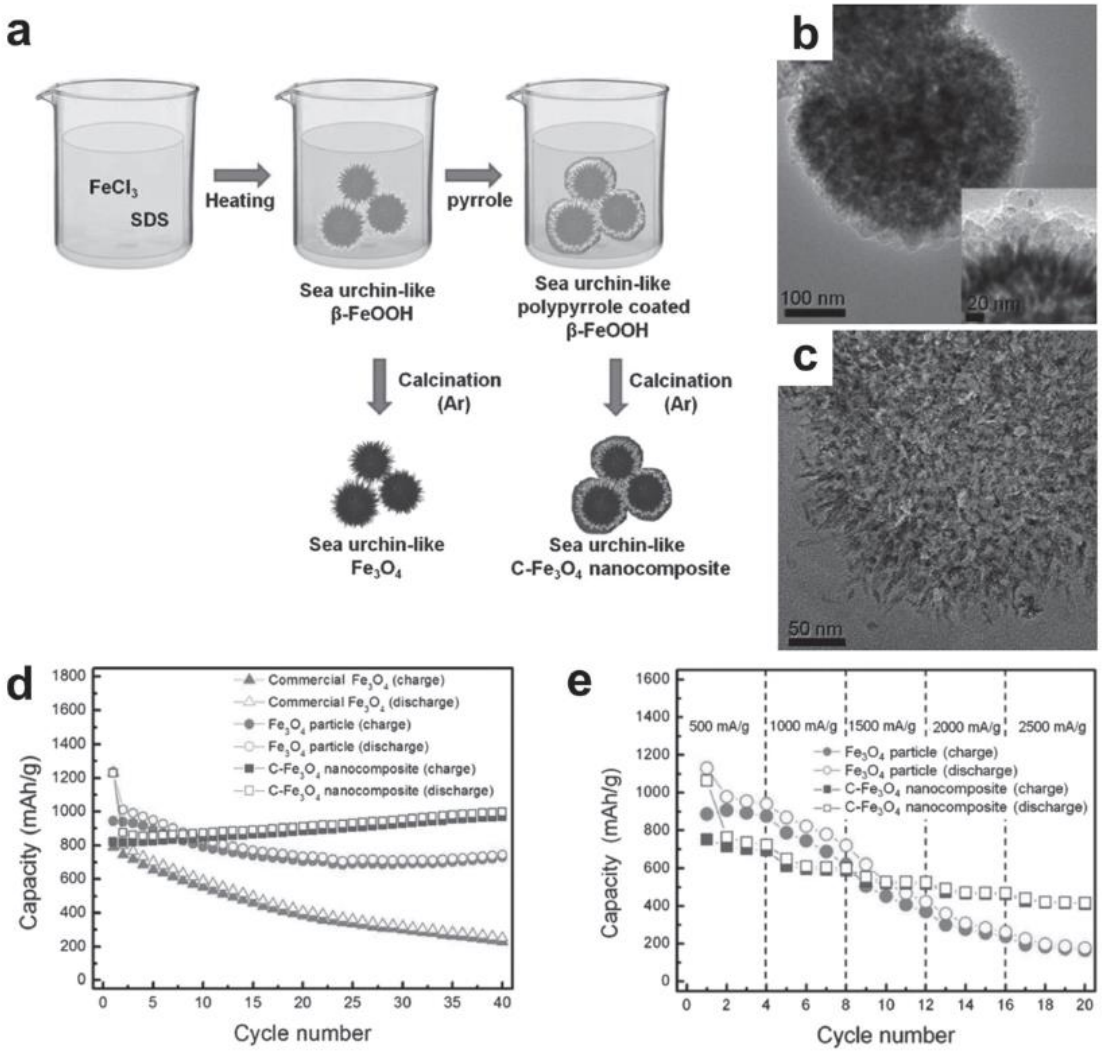

Figure 2.10 (a) Schematic illustration of the preparation of sea-urchin-like porous C-Fe_3O_4 nanoparticles. TEM images of (b) as-prepared, with the inset showing higher magnification, and (c) sectioned C-Fe_3O_4 nanocomposite. (d) Cycling performance and (e) rate performance of the sea-urchin-like porous C-Fe_3O_4 nanoparticles.[72]

stabilizated at a capacity of 1000 mA h g^{-1} at a current density of 100 mA g^{-1} over 100 cycles. Impressively, with the help of this elaborate nanostructure, the C-Fe_3O_4 nanocomposite displayed outstanding rate capability with a reversible capacity as high as 418 mA h g^{-1} at a current density of 2.5 A g^{-1} (Figure 2.12e).[72]

2.3.4 High-capacity Sn anode

Metallic Sn has been widely investigated as one of the best possible anodes for LIBs. Remarkably, a Sn-based composite, Sn-Co-Ti-C, has been commercialized by Sony in its high power Nexelion configuration. Sn presents favorable features, including lower reaction potential (~ 0.3 V vs. Li) and higher theoretical capacity (~ 993 mA h g^{-1} for the reversible formation of $Li_{4.4}Sn$ alloy) compared to the conventional graphitic anodes.[81] The high power capability of Sn compared to graphite is especially worth mentioning. During the lithiation/de-lithiation process, Sn undergoes a (alloying) reaction with metallic Li according to the following equilibrium: $Sn + 4.4Li^{+} + 4.4e^{-} \leftrightarrow Li_{4.4}Sn$. During the lithium ion insertion-extraction process, however, Sn, as well as Sn-based materials, suffers from capacity fading. In addition, the huge volume expansion of the tin results the pulverization of the active materials. Therefore, as suggested in the case of Si-based anode, incorporation of nanosized Sn particles in a sealed matrix could overcome the volume expansion of Sn, which also can enhance the cycling performance of Sn based anodes. A rambutan-like Sn-carbon composite was reported by Lee's group, which was composed of three units: Sn-containing carbon mesospheres, carbon nanotubes with tin inserted completely or partially, and pear-shaped Sn nanoparticles coated with carbon. Due to its unique structure, the nanocomposite maintained a reversible capacity of 311 mA h g^{-1} after 200 cycles.[82]

Furthermore, Chen's group used the aerosol spray pyrolysis method to synthesize a pitaya-like Sn-carbon nanocomposite, as shown in Figure 2.9, in which tin nanoparticles ~8nm in size were homogenously dispersed in the carbon matrix. The first discharge capacity of the as-prepared uniform Sn-carbon spherical nanocomposite was as high as 1007.1 mA h g^{-1} with 63.3% coulombic efficiency. Significantly, it preserved the capacity of 205.3 mA h g^{-1} at the ultrahigh current density of 16000 mA g^{-1} and 410 mA h g^{-1} at the current density of 4000 mA g^{-1} after 1000 cycles.[83]

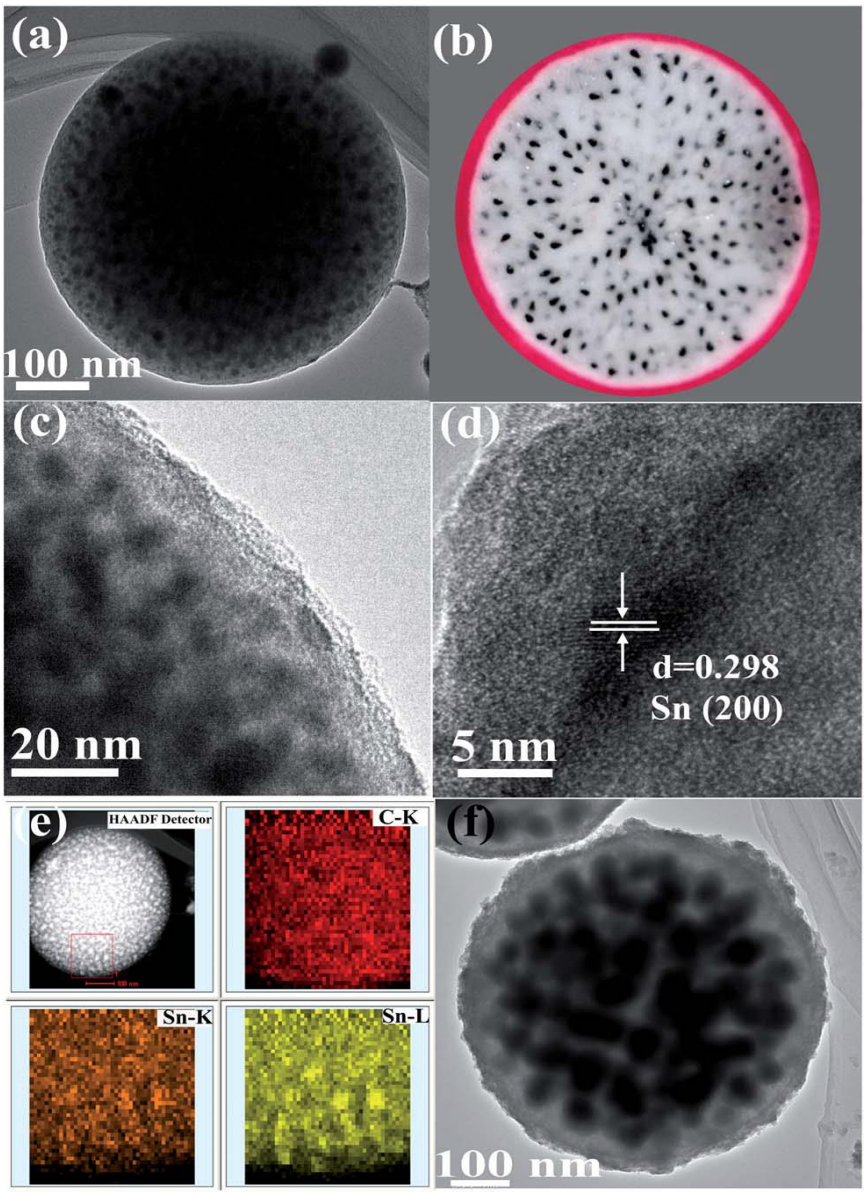

Figure 2.11 (a) Transmission electron microscope (TEM) image of 8 nm-Sn@C, (b) photograph of cross-section of natural pitaya, (c and d) high-resolution TEM images of 8 nm-Sn@C, (e) scanning TEM (STEM) and elemental mapping images of 8 nm-Sn@C, and (f) TEM image of 40 nm-Sn@C.[83]

The aggregation of tin nanoparticles and the isolation of active components from the conductive carbon matrix during the charge-discharge process are the two main obstacles, which cause the capacity degradation of Sn/carbon composite electrodes. To address these issues, methods such as the formation of small nanoparticles and the confinement of tin nanocrystals between graphene layers, have been developed to

realize improved cycling stability.[83] Besides the above-mentioned approaches, numerous studies have demonstrated that 3D graphene frameworks possess a significant advantage in terms of enhancing the cycling lifetime, especially in terms of improvement of the rate capability. Recently, Qin et al. prepared nanocomposites containing with a 3D porous matrix to provide anchoring space for 5-30 nm Sn nanoparticles, which were synthesized by in-situ chemical vapour deposition (CVD) and sealed in graphene shells ~1 nm in thickness. This was achieved by freeze-drying of NaCl particles, which triggered the self-assembly process to form the 3D frameworks and utilize the metal precursors as the catalyst, as shown in Figure 2.10. After calcination in a hydrogen environment, the resultant electrode with its 3D porous architecture had the benefits of a large surface area, enhanced electrical conductivity, and high mechanical flexibility.

As an LIB anode, it exhibited a high rate capacity (1022 mA h g^{-1} at 0.2 C, 865 mA h g^{-1} at 0.5 C, 780 mA h g^{-1} at 1 C, 652 mA h g^{-1} at 2 C, 459 mA h g^{-1} at 5 C, and 270 mA h g^{-1} at 10 C, respectively), and remarkably, a retention of around 96.3% capacity after 1000 cycles as well.[85]

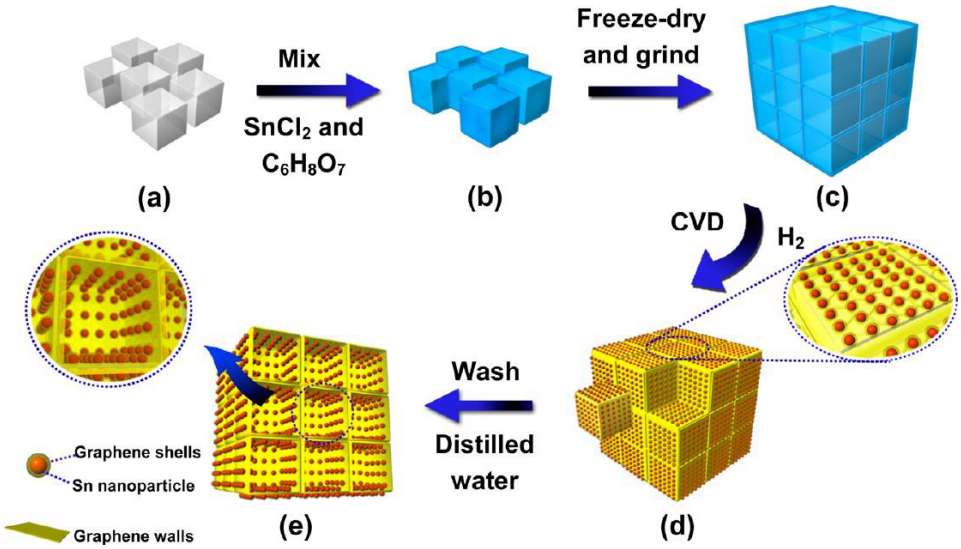

Figure 2.12 Schematic illustration of the in situ CVD process for the formation of 3D Sn@G-PGNWs by using 3D NaCl self-assembly as the template. (a) NaCl particles. (b) $SnCl_2$-$C_6H_8O_7$-coated NaCl particles. (c) $SnCl_2$-$C_6H_8O_7$-coated NaCl self-assembly. (d) Sn@G-GNW-coated NaCl self-assembly. (e) 3D Sn@G – PGNWs.[85]

A hierarchical graphene-Sn@ carbon nanotube (CNT) composite showed a high reversible capacity of over 982 mA h g^{-1} in the first 100 cycles at current density of 100 mA g^{-1} and excellent rate capability performance, with capacity of 828 mA h g^{-1} at the current density of 1000 mA g^{-1} and 594 mA h g^{-1} at the current density of 5000 mA g^{-1}, respectively. This oustanding performance was ascribed to the unique nanostructure, which prevented the agglomeration of graphene and confined the volume expansion of Sn, as well as improving the electrical conductivity by means of the graphene nanosheet (GNS) matrix and the CNT shells. [86]

2.4 Electrolytes for lithium-Ion batteries

Liquid organic solvent-based electrolytes are commercially employed in LIBs, and need to be fulfill the following requirements:[87]

(1) Good solvation of the dissolved lithium salt.
(2) Low viscosity to facilitate ion mobility.
(3) Chemical inertness towards all cell components.
(4) Wide liquid range and high thermal stability.
(5) Environmental benignity and nontoxicity to achieve safe and environmentally friendly batteries.
(6) Suitable interfacial properties to form stable, electronically insulating, but ionically highly conductive SEI films.

As indicated in Table 2.1, state-of-the-art electrolyte solvents consist of a mixture of two kinds of aliphatic carbonates: cyclic carbonates, including ethylene caronate (EC) and PC, which have high dielectric constants (ensuring high salt dissociation), and linear carbonates, such as dimethyl carbonate (DMC), diethyl carbonate (DEC), and ethyl methyl carbonate (EMC), which possess low viscosities and thus ensure suitable ionic conductivity by lowering the overall viscosity of the mixture.[88]

Table 2.1 Physical- and electrochemical properties of state-of-the-art electrolyte solvents for LIBs and a concluding evaluation regarding their safety.[88]

Solvent properties	EC	PC	DMC	DEC	EMC
structure		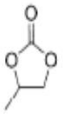	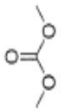	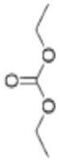	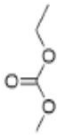
dielectric constant	+	+	−	−	−
viscosity	+	+	−	−	−
melting temperature	+	−	o	−	−
boiling temperature	+	+	−	−	−
flash point	+	+	−	−	−
volatility[b]	−	−	+	+	+
contribution to SEI	+	−	−	−	−
anodic stability	+	+	o	o	o
Σ safety	+	o	−	−	−

[a] + = high, o = medium, − = low. [b] According to NFPA30 (National Fire Protection Association), volatility refers to both flammable (e.g., linear carbonates) and combustible (e.g., cyclic carbonates) liquids.

To enhance the quality of the SEI film, various kinds of additives are mixed into the electrolytes. One of the most widely used compounds is fluorinated ethylene carbonate (FEC), which could effectively enhance the SEI composition and Coulombic efficiency while reducing the first cycle irreversibility. On the other hand, the addition of FEC provides enhanced safety features by reducing flammability compared with non-fluorinated carbonates.[89, 90]

Lithium hexafluorophosphate ($LiPF_6$) is the only commercialized conducting salt used in LIBs. Its solutions have high ionic conductivity (> 10^{-3} S cm^{-1}), a large lithium ion transference number (~0.35), chemical inertness, and satisfactory safety properties. [91-93] Lithium perchlorate ($LiClO_4$), as another common Li salt, offers high electrochemical stability during reduction and oxidation, good ionic conductivity,

and low sensitivity towards moisture.[94] The highly oxidizing nature of ClO_4- leads to a high risk of explosion, however.[95] Therefore, $LiClO_4$ is only utilized for scientific studies but banned from use in LIBs.

2.5 Binders for lithium-ion batteries

Binders can glue all of the components, i.e. conductive additives and active materials, providing a cushion for the dramatic volumetric changes. One potential approach is to use polymeric binders to obtain sustainable electrode integrity, which is able to effectively accommodate the mechanical stress induced during cycling processes. In commercial lithium-ion batteries, poly(vinylidene) fluoride (PVDF) has been widely used as the binder for both the anode and the cathode electrodes due to its good electrochemical stability and high adhesion to the electrode materials and current collectors. It glues through physical surface adsorption and is chemically inert over a big potential range. Nevertheless, PVDF is still limited by its poor cycling performance, especially for high-capacity alloy anodes. This is ascribed to its poor mechanical performance and means that it cannot tolerate the huge volume changes.[96] In addition, PVDF is only soluble in organic solvents, as well as being very expensive and dangerous to humans and the environment;

Another typical binder, carboxymethyl cellulose (CMC), which possesses a high density of hydroxyl and carboxylic acid groups, is effective for alloy anodes. These groups are chemically bonded with the particle surface and form a fixed polymeric layer, leading to an intimate and strong coating of CMC binder on the active material surface.[97] Furthermore, CMC binder is low-cost, presents no pollution problems, and has no requirement for strict control of the processing humidity, which is of great importance for battery production.

Recently, progress has been made on the development of new polymer binders, such as poly(acrylic acid) (PAA),[98] sodium alginate (SA),[99] PAA-CMC,[100] and PAA-gum arabic (GA).[101] The hypothesis behind these developments is that when a two-component adhesive is used as a binder, crosslinking occurs between the two components, which would not only provide high mechanical strength and ductility but also embeds the active particles in the network, both of which may well accommodate the dramatic volumetric changes.

CHAPTER 3 EXPERIMENTAL

3.1 Materials

The materials and chemicals used in this thesis for synthesis, characterization, and electrochemical tests are summarized in Table 3.1. The details of the suppliers are also provided.

Table 3.1 Chemicals and materials used in the thesis.

Materials/Chemicals	**Formula**	**Purity (%)**	**Supplier**
Polyvinylidene difluoride (PVDF)	$(CH_2CF_2)n$	N/A	Sigma Aldrich, Australia
Carbon black	C	Super P	Timcal, Belgium
Milli-Q Water	H_2O	5 ppb (TOC)	Millipore, USA
Ethanol	C_2H_5OH	Reagent	Q-store, Australia
1-methyl-2-pyrrolidinone (NMP)	C_5H_9NO	99.5	Sigma Aldrich, Australia
Polypropylene separator	$(C_3H_6)_n$	Celgard 2500	Hoechst Celanese Corporation, USA
Lithium metal	Li	99.9	Sigma Aldrich, Australia
CR2032 type coin cells	N/A	N/A	China
Electrolyte	$LiPF_6$ in EC/DMC/DEC (3/4/3)+ 5 wt. % FEC	N/A	Novolyte Technologies, USA
Copper foil	Cu	N/A	China
Tin chloride dihydrate	$SnCl_2\ 2H_2O$	99	Sigma Aldrich, Australia
Polyvinylpyrrolidone (PVP)	$(C_6H_9NO)_n$	N/A	Sigma Aldrich, Australia
Ethylene glycol (EG)	$C_2H_6O_2$	99+	Sigma

			Aldrich, Australia
Sodium borohydride	$NaBH_4$	99+	Sigma Aldrich, Australia
Sodium hydroxide	NaOH	99.98	Sigma Aldrich, Australia
Nitric acid	HNO_3	69	Sigma Aldrich, Australia
Oleic acid	$C_{18}H_{34}O_2$	99.5	Sigma Aldrich,

3.2 Experimental procedures

The framework for my research includes the preparation of the designed materials, structural and physical characterization, followed by application of these materials as anodes for LIBs.

3.3 Preparation approaches

The main preparation methods used in the thesis are the hydrothermal, ultrasonication, and heat treament. All the methods are detailed in the following sections.

3.3.1 Hydrothermal method

The hydrothermal method is extremely efficient in crystal growth and nanomaterials synthesis. As shown in Figure 3.1, the device used for hydrothermal synthesis consists of a polytetrafluoroethylene (PTFE) vessel and a stainless steel protector. The composition, morphology, and crystal structure of the products can be affected by many factors, mainly including the volume of the solvent, which relates to the pressure, the concentration of the precursors, the temperature, and the use of a surfactant. Thus, the relevant parameters should be considered in the preparation of desired materials. Generally, the liquid volume is controlled to below 2/3 of the volume of the Teflon reactor.

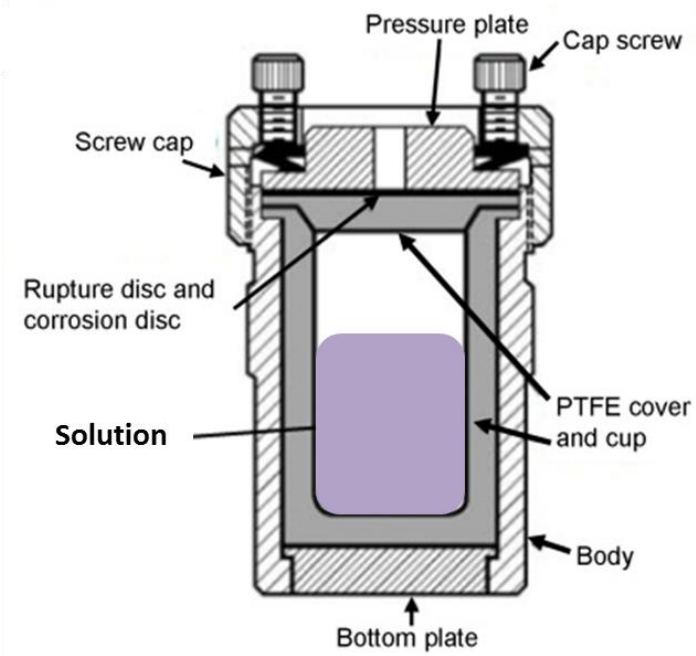

Figure 3.1 Schematic diagram of stainless steel autoclave.

3.3.2 Ultrasonication

In the experiments, ultrasonication was used to improve the mixing and chemical reactions. The parameters of the ultrasonicator (SONICS hand held welder) were adjusted as follows: power output < 18 W, 3 seconds on/off for 3 hours.

3.3.3 Heat-treatment method

Heat-treatment is a critical procedure used to produce high-purity, high-performance solid materials (Figure 3.2). In a typical heat treatment process, one or more volatile precursors are placed in tube furnace, which react and/or decompose on the substrate surface to produce the desired deposit or react with substrate. Meanwhile, volatile by-products are removed by gas flow through the reaction chamber. The advantages of heat treatment include a high deposition rate and high degree of control. Tuning the process is can be easily achieved by manipulating the vapour flows in the coating zone and the heat-treatment temperature.

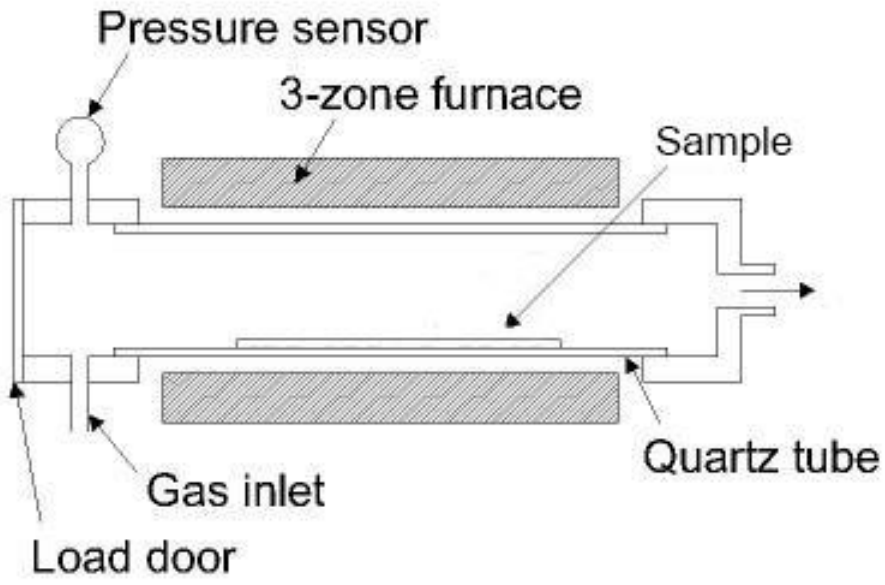

Figure 3.2 Schematic diagram of heat treatment in a three-zone tube furnace.

3.4 Characterization and measurement methods

3.4.1 X-ray Diffraction (XRD)

X-ray diffraction (XRD) is a direct and powerful experimental technique to determine the structural characterization of materials, in which the crystalline atoms cause a beam of X-rays to diffract into many specific directions. In the X-ray diffractometer, the copper anode is irradiated with a beam of high-energy electrons that is accelerated by a high voltage electric field to a very high speed. A small Be window in the X-ray tube allows the X-rays to exit the tube with little attenuation, while maintaining the vacuum seal required for the X-ray tube operation. X-rays can be considered waves of electromagnetic radiation, and crystals are regular arrays of atoms. Atoms scatter X-ray waves through the atoms' electrons. A regular array of scatterers produces a regular array of spherical waves. The scattering from all the different sets of planes results in a pattern unique to the crystal structure of a given compound. Bragg's law describes the diffraction condition from planes with spacing, d:

$$2d\sin\theta = n\lambda \quad (3.1)$$

where d is the distance between diffracting plans, λ is the wavelength of the incident X-ray beam, n is any integer, and θ is the angle of incidence experienced by the X-ray beam reflection from the faces of the crystal. In this work, only X-ray powder diffraction was used. The powder sample is loaded onto a small disc-shaped sample holder, which is put on one axis of the diffractometer and tilted by an angle θ, while a detector rotates around it on an arm at a 2θ angle.

The XRD devices used in this thesis are a GBC MMA diffractometer and a Bruker D8-Advanced X-ray Diffractometer in UOW and NTU, respectively. All the XRD devices use Cu Kα radiation, λ = 1.5406 Å and graphite monochromators.

3.4.2 Scanning electron microscopy (SEM)

The scanning electron microscope (SEM) is a type of electron microscope to scan a sample surface with a high-energy beam of electrons. In a typical SEM, an electron beam is emitted from an electron gun fitted with either a tungsten or LaB_6 filament cathode, or an SEM configured with a tungsten field emitter (an FSEM). The electron beam, which typically has an energy ranging from 0.2 to 40 keV, is focused by one or two condenser lenses to a spot about 0.4 nm to 5 nm in diameter. The beam passes through pairs of scanning coils or pairs of deflector plates in the electron column, typically in the final lens, which deflects the beam with respect to the x and y axes so that it scans in a raster fashion over a rectangular area of the sample surface. The electrons interact with the atoms that make up the sample, producing signals that contain information about the sample's surface topography, composition, and other properties, such as electrical conductivity. The types of signals produced by an SEM include secondary electrons, back-scattered electrons (BSE), characteristic X-rays, light specimen currents, and transmitted electrons. Secondary electron detectors are common used in all SEM, which can offer very high resolution images.

The morphology and structure of samples in this thesis were characterized with a field-emission scanning electron microscope (FESEM; JEOL 7500 in UOW).

3.4.3 Transmission electron microscopy (TEM)

Transmission electron microscopy (TEM) is a technique to observe sample's morphology, lattice spacing, crystal orientation and electronic structure. A beam of electrons is transmitted through an ultra-thin specimen, interacting with the specimen as it passes through, and then an image is formed from the interaction. TEM is capable of imaging at a significantly higher resolution than light microscopes, owing to the small de Broglie wavelength of electrons. Selected area electron diffraction (SAED) is a crystallographic experimental technique that can be performed inside a transmission electron microscope (TEM). The TEM consists of an emission source, which may be a tungsten filament or a lanthanum hexaboride source. By applying a high voltage source (typically 100 – 300 kV), the gun will begin to emit electrons either by thermionic or field electron emission into a vacuum. This extraction is usually aided by the use of a Wehnelt cylinder. Once extracted, the upper lenses of the TEM allow for the formation of the electron probe to the desired size and location for later interaction with the sample. TEM specimen stage designs include airlocks to allow for insertion of the specimen holder into the vacuum with minimal increase in pressure in other areas of the microscope. Standard sized TEM samples are a typically 3.05 mm in diameter. For the case of powder samples, these are commonly dispersed on a support such as thin carbon film, holey carbon or lacey carbon, the support being attached to a 3.05 mm diametr thin meshed metal grid with typically 50-200 μm mesh spacing. The TEM grid with sample is placed on the sample holder, which is paired with the specimen stage.

The powder samples for TEM were dispersed in ethanol and then loaded onto a holey carbon support film on a copper mesh grid, the advantage of holey carbon being that powder particles located over the holes can be imaged and analysed without interference from the sample support. The TEM used in this thesis was a TEM, JEOL ARM-200F. Elemental mapping was performed on the X-ray spectrometer attached to the JEOL ARM-200F instrument.

3.4.4 Thermogravimetric Analysis (TGA)

Thermogravimetric analysis or thermal gravimetric analysis (TGA) is a method of

thermal analysis that is performed on samples to determine change in weight in relation to change in temperature. Commonly, it is used to determine selected characteristics of materials that exhibit mass loss or increase because of decomposition, oxidation, or loss of volatiles. Differential scanning calorimetry (DSC) can measure both heat flow and weight changes in materials as a function of temperature or time in a controlled atmosphere. The two measurements are combined together to investigate the changed properties. In this master work, TGA was used to determine the carbon contents in the carbon composite materials. TGA was carried out in air atmosphere using SETARAM Thermogravimetric Analyzer (France) in UOW.

3.4.5 Brunauer Emmett Teller (BET)

In 1938, Stephen Brunauer, Paul Hugh Emmett, and Edward Teller published an article about their BET (denoted from the first initials of their family names) theory for the first time.[4] The BET method is an important analysis technique to explain the physical adsorption of gas molecules on a solid surface and measure the specific surface area of a material. The BET surface area was calculated using experimental points at a relative pressure of P/P^0 = 0.05 – 0.25. The pore size distribution was calculated by using the Barrett-Joyner-Halenda (BJH) method. The total pore volume was estimated by the amount of nitrogen adsorbed at a relative presure (P/P^0) of 0.99. In this work, nitrogen sorption was measured by using a Quantachrome Instruments Autosorb AS-6B in NTU or a Quanta Chrome Nova 1000 in UOW in liquid nitrogen.

3.4.6 Raman spectroscopy

Raman spectroscopy is a spectroscopic technique for the study of the vibrations of chemical bonds and symmetry of molecules, commonly used in chemistry to identify materials.[5] In a Raman spectrometer, a laser light interacts with molecular vibrations, phonons, or other excitations, resulting in the energy of some laser photons being shifted up or down. The shift in energy gives information about the phonon modes in the system. The Raman spectra in this thesis work were collected on a JOBIN Yvon Horiba Raman Spectrometer model HR800, employing a 10 mW helium/neon laser at 632.8 nm.

3.5 Electrode fabrication and cell assembly

3.5.1 Electrode preparation

The working electrodes were prepared by mixing the active materials, a conductive agent (carbon black, Super-P-Li), and a binder (PVDF or CMC or AB glue) in specific ratios to form a homogeneous slurry, which was uniformly pasted onto Cu foil. The prepared working electrodes were dried in a vacuum oven at 120 °C (PVP and AB) for 12 h and 80 °C (CMC) for 12 h. The dried electrodes were punched into discs with a diameter of 0.96 cm after rolling-press procedure. The loading mass of the active materials in the work is 08-1.0 mg cm^{-2}. The discs were ready to be assembled into a testing cell in a argon filled glove box.

3.5.2 Cell assembly

The cell assembly was carried out in an Ar-filled glove box. 2032-type coin cells or Swagelok-type cells were used with lithium foil as both the counter and reference electrodes and a porous polypropylene film as separator. The specific capacity was calculated based on the mass of active materials in the electrode. A schematic diagram of the coin-type cell is shown in Figure 3.3. The electrolyte was added on both sides of the separator. After tight sealing, the cells were aged 12 hours before electrochemical testing.

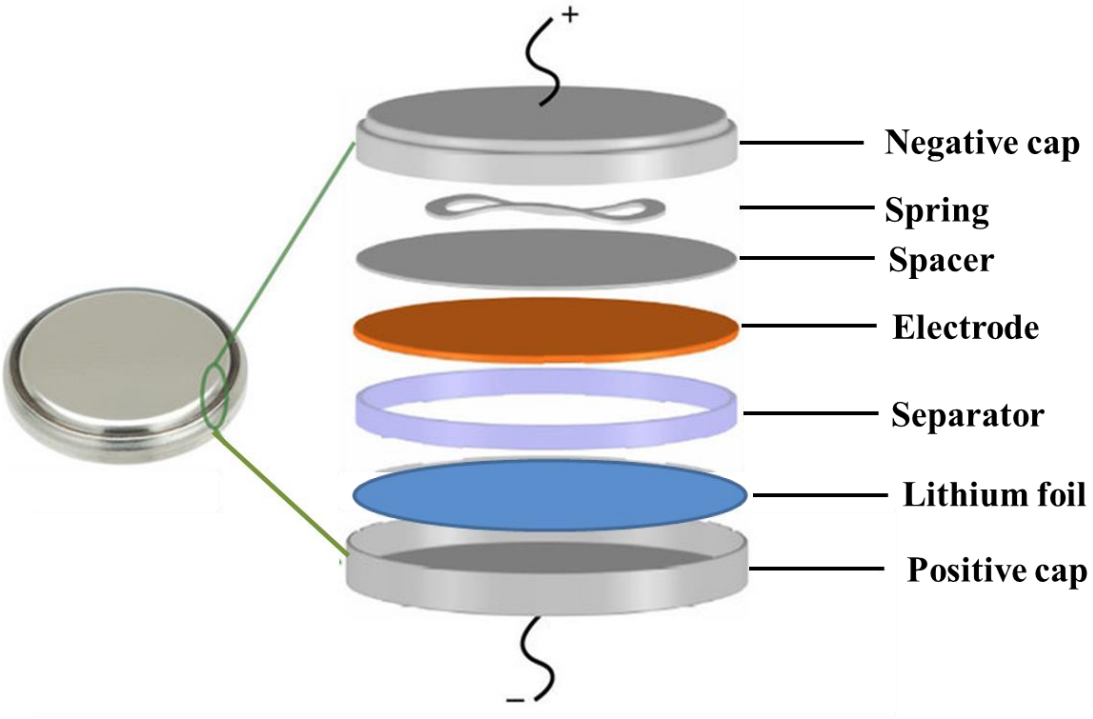

Figure 3.3 Schematic diagram of a 2032-type testing cell.

3.6 Electrochemical measurements

Electrochemical performance of LIBs was evaluated by different measurement technologies, including cyclic voltammetry, galvanostatic charging/discharging, and electrochemical impedance microscopy.

3.6.1 Cyclic voltammetry (CV)

Cyclic voltammetry (CV) is an electrochemical technique used to measure the current that develops in an electrochemical cell under conditions where the voltage is in excess of that predicted by the Nernst equation. The CV testing for coin cells is based on the two-electrode model, in which lithium foil act as both reference electrode and counter electrode. A pairs of peaks would be observed at both anodic and cathodic curves when a redox reaction occurs. The CV data were acquired on a Biologic VMP-3 electrochemical workstation.

3.6.2 Galvanostatic electrochemical testing

The apparatus for galvanostatic testing is a measurement device capable of maintaining a constant current density. The cells can also be tested for rate capability at different current densities. The instruments used here to obtain the data were a Neware battery tester (China) or a Land battery tester.

3.7 Nomenclature and symbols used in the thesis

3.7.1 Nomenclature

Table 3.2 List of Abbreviations

List of Abbreviations	
Abbreviation	**Full name**
BET	Brunauer-Emmett-Teller
PVDF	Polyvinylidene fluoride
TGA	Thermogravimetric analysis
a.u.	Arbitrary unit
SEI	Solid electrolyte interphase
SEM	Scanning electron microscopy
LIBs	Lithium ion batteries
NMP	1-methyl-2-pyrrolidinone
CNT	Carbon nanotube
CV	Cyclic voltammetry
DMC	Dimethyl carbonate
EC	Ethylene carbonate
HRTEM	High-resolution transmission electron microscopy
EDX	Energy dispersive x-ray spectroscopy
EIS	Electrochemical impedance spectroscopy
EV	Electric vehicle
HEV	Hybrid electric vehicle
FE-SEM	Field-emission scanning electron microscopy

SAED	Selected area electron diffraction
XRD	X-ray diffraction
JCPDS	Joint Committee on Powder Diffraction Standards
TEM	Transmission electron microscopy

3.7.2 Symbols

Table 3.3 List of Symbols

Symbol	**Name**	**Unit**
2θ	Peak position of XRD	°
C-rate	Charged or discharged rate	mA
Q_c	Specific charge capacity	mA h g^{-1}
Q_d	Specific discharge capacity	mA h g^{-1}
R_{ct}	Charge transfer resistant	Ω
S_{BET}	Specific BET surface area	m^2 g^{-1}
S_E	Electrochemically active surface area	m^2 g^{-1}
t	Time	h or s
T	Temperature	K or °C
λ	X-ray wavelength	Å
L	Crystal size	nm
m	Active material weight	g
N	Avogadro's number = 6.022×10^{-23}	mol^{-1}
P	Equilibrium pressure	P
P_0	Saturation pressure	P
Q	Specific capacity	mA h kg^{-1}

CHAPTER 4 INTEGRATED ANODE VIA GLUING TIN NANOPARTICLES ON SUBSTRATE FOR HIGH-PERFORMANCE LITHIUM ION BATTERIES

Based on recent progress in the development of complex polymer binders, an epoxy resin (Part A) – amine (Part B) glue was selected as an effective binder for integration with tin in the fabrication of a new tin anode. The obtained electrode (denoted as Sn-AB) realizes the homogeneously dispersion of Sn active nanoparticles in AB binder via formation of coordination complex around the oxidized surface of Sn nanoparticles during the curing process of Part A and Part B. The electrode exhibits a stable capacity of ~ 400 mA h g^{-1} over 100 cycles and superior rate capability for fast charge/discharge processes (~ 235 mA h g^{-1} at 5 A g^{-1} in comparison of ~ 475 mA h g^{-1} at 0.2 A g^{-1}). To the best of our knowledge, this is the best performance of pure Sn nanoparticles with various binders ever reported as far. The Sn-AB electrode possesses intimate particle/particle cohesion and good laminate/current collector adhesion, which effectively enhances the utilization of active materials and integration of electrode, and prevents the particle pulverization/ agglomeration during cycling, thereby responsible for the improvement of the Sn electrode in terms of practically accessible capacity and rate capability. Moreover, this favorable AB binder is also expected to be extensively applied into other anode and cathode materials for energy storage and conversion applications.

4.1 Introduction

Ever-growing energy demands and the depletion of fossil-fuel resources are accelerating the pursuit of sustainable energy alternatives. Lithium-ion batteries (LIBs) are expected to find major applications in both portable devices and electric vehicles.[102] Therefore, it carries ongoing great significance to develop high-capacity, low-cost, and environmentally-friendly electrode materials,[103-107] especially on the anode side due to the limited capacity of conventional graphite anode (~ 372 mA h g^{-1}, corresponding to LiC_6). Tin, with about three times higher capacity (~ 990 mA h g^{-1}, corresponding to $Li_{22}Sn_5$) and higher electronic conductivity, is believed to hold great promise for replacing graphitic carbon. However, its practical application in Li-

ion batteries has been severely limited by rapid capacity decay due to the large volume variation of ~ 260 % during charge/discharge processes.[108]

To address this intractable problem, much effort has been directed towards the design and synthesis of Sn-based materials. One approach is to prepare Sn-based alloys with an inactive phase such as Cu,[109] Ni,[110] or Co,[111] which could effectively buffer the volume variation of Sn. Another approach is to prepare composites consisting of carbonaceous matrixes and nanosized Sn particles, including Sn-C composites,[112-114] Sn-carbon nanotube (CNT) composites,[115, 116] and Sn-graphene composites,[117, 118] which could enhance the overall conductivity of the active materials and accommodate the volume changes of Sn. The drastic volume expansion, however, would still unavoidably disrupt the anode's integrity and induce the electrode surface cracking, leading to excessive side reactions and fast capacity fade.

A potential solution is to use polymeric binders to obtain sustainable electrode integrity. Binder can glue all of the components, i.e. conductive additives and active materials, providing cushion for the dramatic volumetric changes. The conventional polymer binder polyvinylidene fluoride (PVDF) is often used for graphite anodes and most metal oxide cathode materials, and it glues via physical surface adsorption and is chemically inert over the high potential range. Nevertheless, PVDF is limited by poor cycling performance for high-capacity alloy anodes, because it has poor mechanical performance and cannot tolerate the huge volume changes.[119] Another typical binder carboxymethyl cellulose (CMC) is effective in alloy anodes, and it possesses a high density of hydroxyl and carboxylic acid groups. These groups can chemically bond to the particle surface and to form a fixed polymeric layer, leading to an intimate and strong coating of CMC binder on the active material surface.[120]

Recently, progress has been made on the development of new polymer binders, such as poly(acrylic acid) (PAA),[121] sodium alginate (SA),[122] PAA-CMC,[123] and PAA-gum arabic (GA).[124] A hypothesis made herein is that when a two-component adhesive is used as a binder, crosslinking occurred between the two components would not only provide high mechanical strength and ductility but also embed the

active particles in the network, both of which may accommodate well the dramatic volumetric changes. We thus explored a commercial adhesive as a binder (AB) in this study, which consists of epoxy resin- diglycidyl ether of bisphenol A (DGEBA), denoted as Part A, with epoxide equivalent weight 182 ～196 g per equiv and amine hardener (Part B).

Herein, ultrafine Sn nanoparticles have been prepared via a facile chemical decomposition method taking advantage of auxiliary ultrasonication dispersion. Pure Sn nanoparticles rather than Sn-based composites have been selected in order to highlight the effect of the binder on the anode cycling performance. Significantly, because of benefits from the charge transfer occurring between nitrogen and oxygen atoms, the selected AB binder can form a coordination complex around the oxidized surface of Sn nanoparticles, which realizes intimate particle/particle cohesion and good laminate/current collector adhesion during the curing process, thereby responsible for the improvement of the Sn electrode in terms of practically accessible capacity and rate capability. To the best of our knowledge, this is the first reported to use commercial AB glue as an electrode binder. The Sn electrode with AB binder delivers a stable capacity of ~ 400 mA h g^{-1} over 100 cycles and excellent rate capability (retaining 230 mA h g^{-1} at 5 A g^{-1}), both of which outperform the electrode made by conventional CMC binder. The unique electrode integrated with the aid of AB binder can well tolerate the serious mechanical stress caused by the large volume variations of Sn nanoparticles, and this resulted in excellent cycling performance and rate capability.

4.2 Experimental

4.2.1 Preparation of tin nanoparticles

Solution A was first prepared by dissolving 0.76 g $SnCl_2 \cdot 2H_2O$ and 5 g polyvinylpyrrolidone (PVP) in 50 ml ethylene glycol (EG); solution B was prepared by dissolving 0.15 g $NaBH_4$ in 125 ml H_2O and 125 ml ethanol. Then, solution B was placed into an ultrasonic bath, which was followed by the dropwise addition of solution A to solution B over 30 minutes. A white precipitate can be observed at this stage due to the hydrolysis of $SnCl_2 \cdot 2H_2O$ and the reduction of $NaBH_4$. The obtained white mixture was further ultrasanicated for 30 minutes. The white precipitate was collected and washed three times with deionized water and ethanol. Finally, the Sn nanoparticles were obtained after drying the precipitate in a vacuum oven at 50 °C overnight.

4.2.2 Physical characterization

The morphology of the ultrafine Sn nanoparticles was investigated by transmission electron microscopy (TEM; JEOL 2011, 200 keV) and scanning electron microscopy (SEM; JEOL JEM-7500FA). The microstructure was characterized by powder X-ray diffraction (XRD; GBC MMA diffractometer) with Cu Kα radiation at a scan rate of $2\ ^{o}\,min^{-1}$. X-ray photoelectron spectroscopy (XPS) was carried out on a VG Scientific ESCALAB 2201XL instrument using Al Kα X-ray radiation and fixed analyzer transmission mode. The toughness of the binders was investigated on an INSTRON 5943. The curing process was studied by Fourier transform infrared microspectroscopy (FTIR, Shimadzu AIM8000 FT-IR spectrometer). Ultrathin sections were microtomed from samples (embedded by epoxy) using a Leica Ultracut S microtome equipped with a diamond knife, and were collected on 200-mesh copper grids.

4.2.3 Electrochemical measurements

The electrode slurry was prepared by fully mixing 80 wt. % Sn nanoparticles, 10 wt. % Super P, and 10 wt. % binder (AB, CMC, and PVDF). For the Sn nanoparticles electrode with AB binder (Sn-AB), stoichiometric Sn nanoparticles and Super P were added into the epoxy (A) solution with N-methyl-2-pyrrolidone (NMP) solvent and

initially mixed for 5 minutes using a planetary mixer (KK-250S), which was then followed by adding the appropriate amount of amine hardener (B) and further mixing for another 8 minutes. The obtained slurry was pasted onto copper foil with a doctor blade in a thickness of 100 μm, followed by drying in a vacuum oven at 120 °C overnight. For comparison, the Sn NP electrodes with CMC binder (Sn-CMC) and PVDF binder (Sn-PVDF) were prepared by drying the corresponding slurry in a vacuum oven at 80 and 120 °C overnight, respectively. The working electrodes were prepared by punching the electrode film into discs 1.4 cm in diameter. The electrochemical measurements were conducted by assembling coin-type half cells in an argon-filled glove box. Lithium foil was utilized as both reference and counter electrode. The electrodes were separated by a porous polypropylene separator. The electrolyte was 1.0 M $LiPF_6$ in 3:4:3 (weight ratio) ethylene carbonate (EC) / dimethyl carbonate (DMC) / diethyl carbonate (DEC), with 5 wt. % fluoroethylene carbonate (FEC) additive from Novolyte Technologies. The electrochemical performance was tested on a Land Battery Test System with a cut-off voltage range from 0.005 V to 1.5 V (vs. Li/Li^+). Cyclic voltammetry and impedance testing were performed using a Biologic VMP-3 electrochemical workstation from 0.005 V to 1.5 V at a sweep rate of 1 mV s^{-1}.

4.3 Characterizations of morphology and structure

As shown in the schematic illustration (Figure 4.1), the Sn nanoparticles and conductive carbon were first evenly wrapped up in the epoxy (Part A) with NMP solvent, which was followed by adding an appropriate amount of ammine hardener (Part B). *Via* the cross-linking

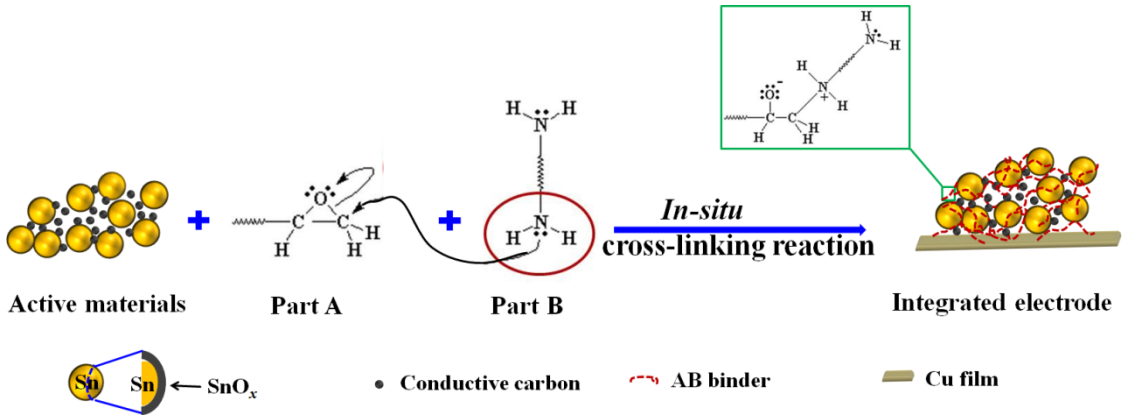

Figure 4.1 Schematic representation of the construction of integrated Sn-AB electrode via the *in-situ* cross-linking reaction between the epoxy and the amine hardener.

reaction, the thus-formed epoxy-amine (AB) binder becomes well entangled with all the components of the electrode through long chains. The evolution of the AB binder is investigated *via* FTIR (Figure 4.2). Compared with epoxy, two bands at 3056 and 915 cm^{-1} disappear in the AB binder, indicating the opening of epoxy rings; the generated band at 1638 cm^{-1} is ascribed to the formation of OH groups in the AB binder, further confirming the occurrence of cross-linking reaction.[125]

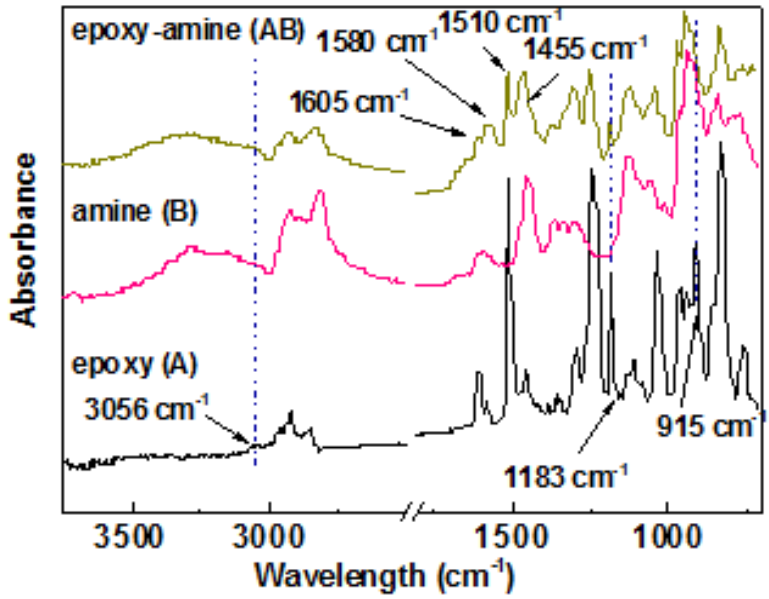

Figure 4.2 The FTIR spectra of epoxy, amine and crosslinked epoxy-amine mixture

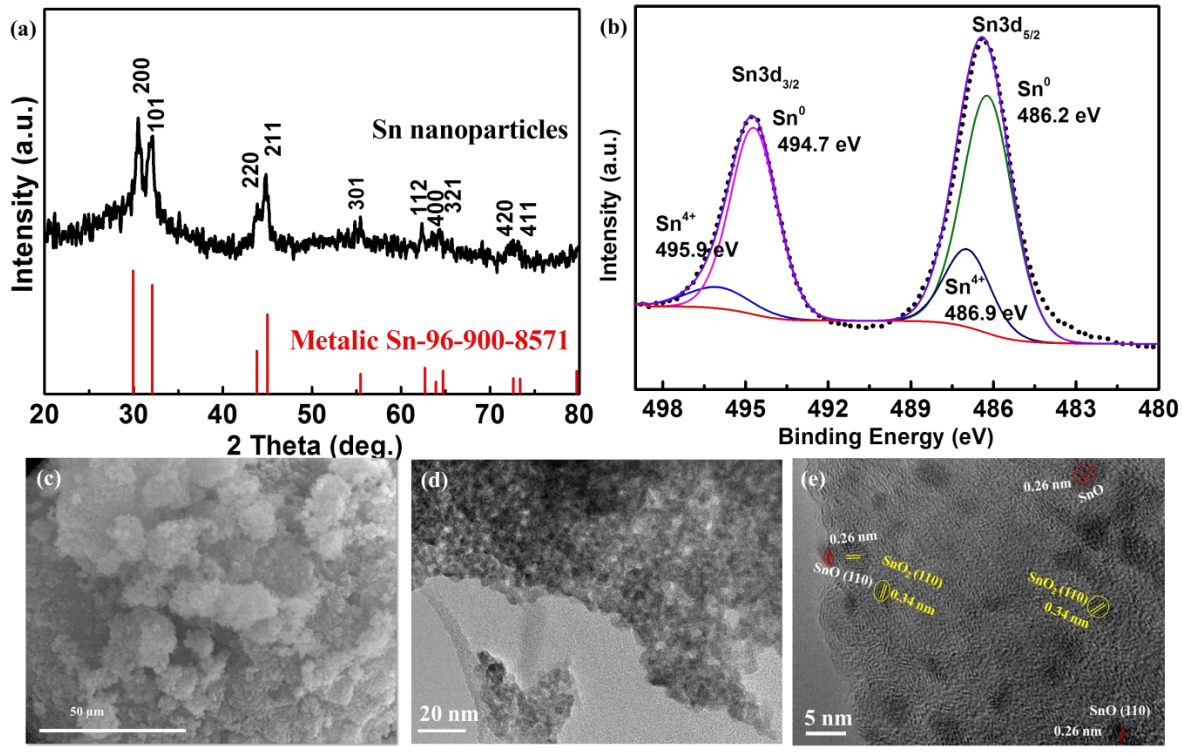

Figure 4.3 XRD, XPS and Electron Microscopy of tin anode; (a) XRD pattern, (b) Sn 3d XPS spectrum, (c) SEM, (d) TEM, and (e) high-resolution TEM images of Sn nanoparticles.

Figure 4.3 shows representative XRD, XPS, SEM and TEM results obtained from the fabricated tin anode. An X-ray diffraction (XRD) pattern obtained from the as-prepared material is presented in Figure 4.3a, which can be well indexed to crystalline metallic Sn (JCPDS card No. 96-900-8571). The broadened peaks indicate the small crystal size of the as-obtained Sn nanoparticles. Furthermore, the high-resolution Sn 3d spectrum collected *via* X-ray photoelectron spectroscopy (XPS) is presented in Figure 4.3b. Two peaks located at 486.2 ($3d_{5/2}$) and 494.7 ($3d_{3/2}$) are assigned to the binding energies for Sn^0 (metallic Sn). Two peaks at 486.9 and 495.9 eV with low peak area proportions correspond to the binding energies of Sn $3d_{5/2}$ and Sn $3d_{3/2}$ of Sn^{4+}, respectively, indicating the presence of SnO_x from the surface oxidization of Sn.[126] The existence of Sn-O bonding facilitates the formation of coordination complex between binder and the oxidized surface of Sn nanoparticles and thus form a multidimensional, high-strength polymer network, which should improve the interfacial strength between the binder and the active material. The morphology of Sn nanoparticles was characterized via transmission electron microscopy (TEM) and scanning electron microscopy (SEM). As shown in Figure 4.3d, it can be seen that a myriad of Sn particles have agglomerated together owing to the ultra-small nanosize of particles, consistent with the SEM image of Sn nanoparticles (Figure 4.3c). The as-obtained Sn nanoparticles are distributed with an average diameter of around 3 nm, which is clearly illustrated in the high-resolution TEM (HRTEM) image (Figure 4.3e), which also shows lattice spacings consistent with formation of Sn nanoparticles. Moreover, it should be pointed out that the Sn samples are highly amorphous, which increase the difficulty to observe any lattice spacing corresponding to metallic Sn. In addition, several particles show crystallinity with *d*-spacings of 0.26 and 0.34 nm, which correspond to the (110) planes of SnO and SnO_2, respectively, indicating the surface oxidization of the as-prepared Sn ultrafine nanoparticles.[127]

4.4 Electrochemical performance

To highlight the functions of this developed AB binder, the conventional CMC and PVDF binders were utilized to prepare Sn-CMC and Sn-PVDF electrodes as comparison. As shown in Figure 4.4a, the reversible capacities of Sn-AB, Sn-CMC, and Sn-PVDF are 660, 625, and 436 mA h g^{-1}, respectively. In contrast, Sn-CMC and Sn-PVDF, the initial Coulombic efficiency of Sn-AB is quite low (~ 40 %), which is ascribed to the formation of solid electrolyte interface (SEI) film and irreversible reactions, especially the possible side-reaction between AB binder and Li ions. The absence of multi-plateau curves for the three electrodes during the initial discharge process indicates that the alloying steps have overlapped and become indistinguishable due to the ultra-small nanoscale of Sn particles. The charge/discharge profiles of Sn-AB, Sn-CMC, and Sn-PVDF at selected cycles are displayed (Figure 4.4b, c and d). PVDF only bound Sn particles *via* weak surface adherence, thereby leading to poor binding force.[128] As predicted, the Sn-PVDF electrode shows the lowest charge capacity and the most serious capacity decline. The binding force of Sn-CMC is far stronger than that of Sn-PVDF due to the hydrogen bonding between the carboxylic groups of CMC and the active nanoparticles,[129] As predicted, the Sn-PVDF electrode shows the lowest charge capacity and the most serious capacity decline. The binding force of Sn-CMC is far stronger than that of Sn-PVDF due to the hydrogen bonding between the carboxylic groups of CMC and the active nanoparticles,[130] resulting in enhanced capacity and cycling stability. In contrast, Sn-AB shows the highest reversible capacity and maintains the best capacity retention, which is due to the exceptional bonding capability of AB binder. Through the cross-linking reaction between Part A and B, the obtained polymeric binder could well entangle all of the active particles via forming coordination complex around the oxidized surface of Sn nanoparticles. Similarly, the cyclic voltammograms curves (CVs) of Sn-AB show the highest repetition with intensive anodic and cathodic peaks, indicating the best electrode kinetics (Figure 4.5). The Sn-AB electrode, therefore, is anticipated to deliver superior electrochemical properties.

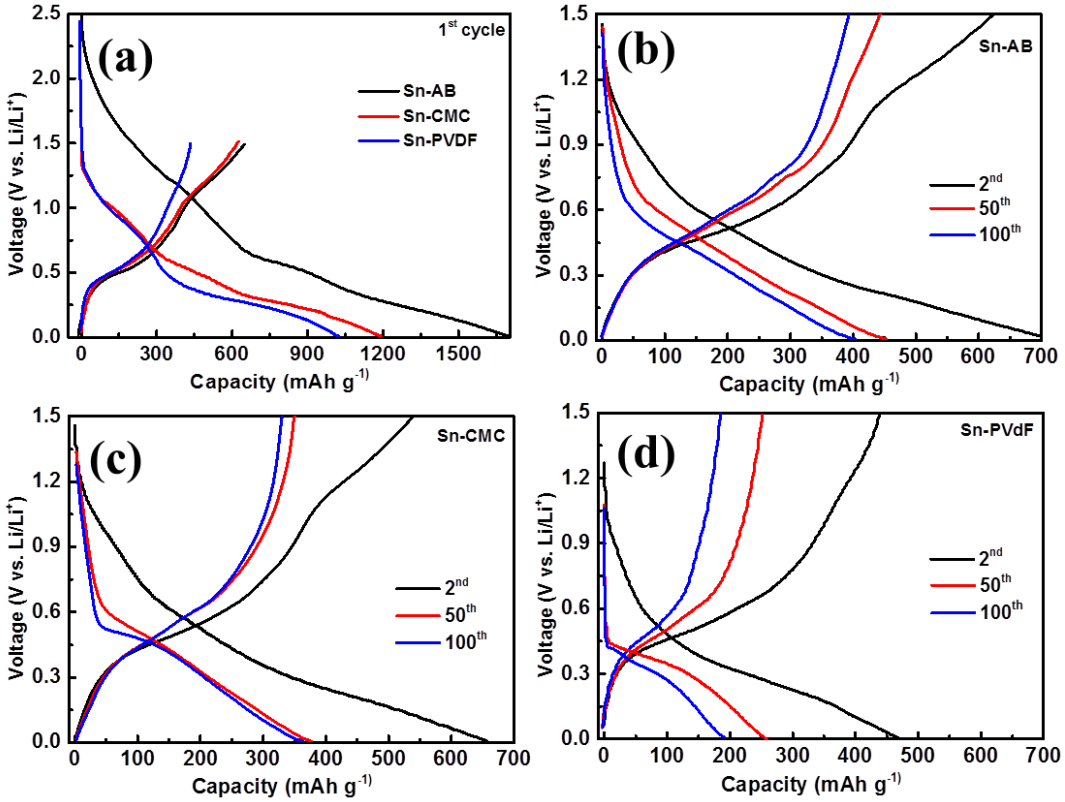

Figure 4.4 (a) Charge/discharge curves at the first cycle of Sn-AB, Sn-CMC, and Sn-PVDF; Charge/discharge profiles for selected cycles of (b) Sn-AB, (c) Sn-CMC, and (d) Sn-PVDF at a current density of 0.1 A g^{-1} within a potential window between 0.005 and 1.5 V.

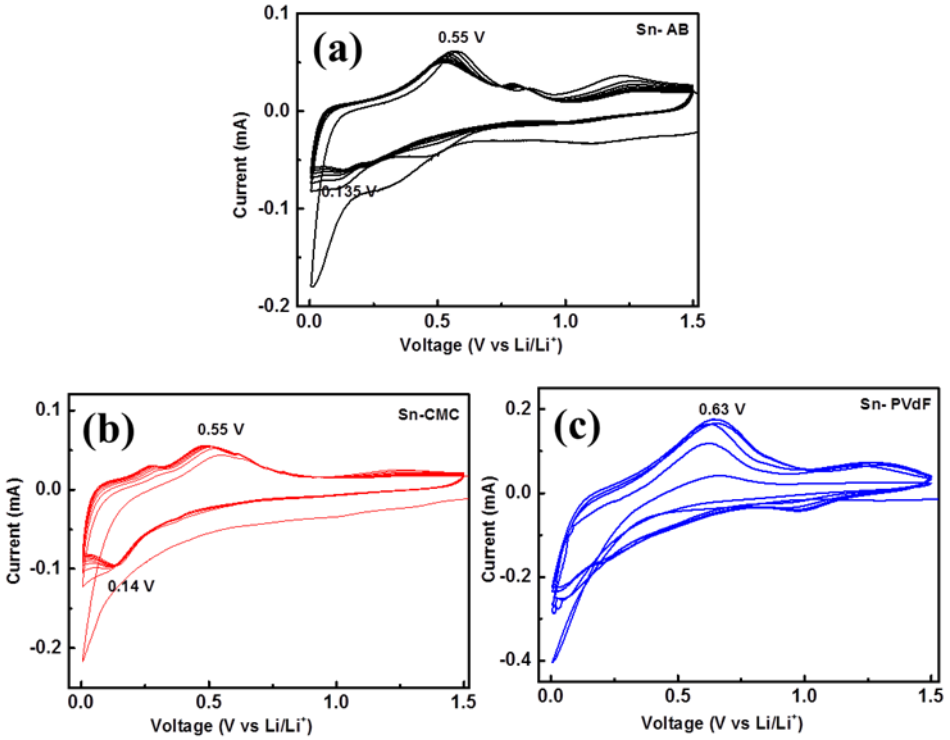

Figure 4.5 Cyclic voltammograms of the electrodes at a scan rate of 0.1 mV s^{-1} within the voltage range of 0.005 to 1.5 V for (a) Sn-AB, (c) Sn-CMC, and (e) Sn-PVDF.

As displayed in Figure 4.6a, the Sn-AB shows excellent cycling stability and high capacity retention, delivering a reversible capacity of 400 mA h g^{-1} over 100 cycles. In comparison, Sn-CMC demonstrates a moderate performance in term of stability and capacity, retaining a reversible capacity of 355 mA h g^{-1}. Sn-PVDF electrode unsurprisingly undergoes rapid capacity decay, only retaining a reversible capacity of 192 mA h g^{-1} after 100 cycles. Impressively, the Sn-AB electrode delivers prevailing rate capability when tested at various current densities from 0.1 to 5 A g^{-1} (Figure 4.6b). The Sn-PVDF electrode shows the lowest capacity and fastest capacity decline with increase in current density. The reversible specific capacities of both Sn-AB and Sn-CMC decay gradually, with similar performance from 0.1 to 1 A g^{-1}. It is noteworthy that Sn-AB electrode delivers much higher capacity than Sn-CMC at the faster charge/discharge processes, respectively leading to capacity retention of ~ 235 and ~ 180 mA h g^{-1} at 5 A g^{-1}. When the current rate returns back to 0.1 mA g^{-1}, the capacity of Sn-AB and Sn-CMC recovers to 500 and 412 mA h g^{-1}, respectively. The

electrode of ultrafine Sn nanoparticles with AB binder exhibits the best electrochemical performance in terms of cycling performance and rate capability so far. As shown in Figure4.6c, It is clear that Sn-PVDF in this work shows much higher capacity retention than the reported commercial Sn nanoparticlas with PVDF binder (C-Sn-PVDF);[119, 130] the Sn-CMC

Figure 4.6 (a) Charge/discharge curves at the first cycle of Sn-AB, Sn-CMC, and

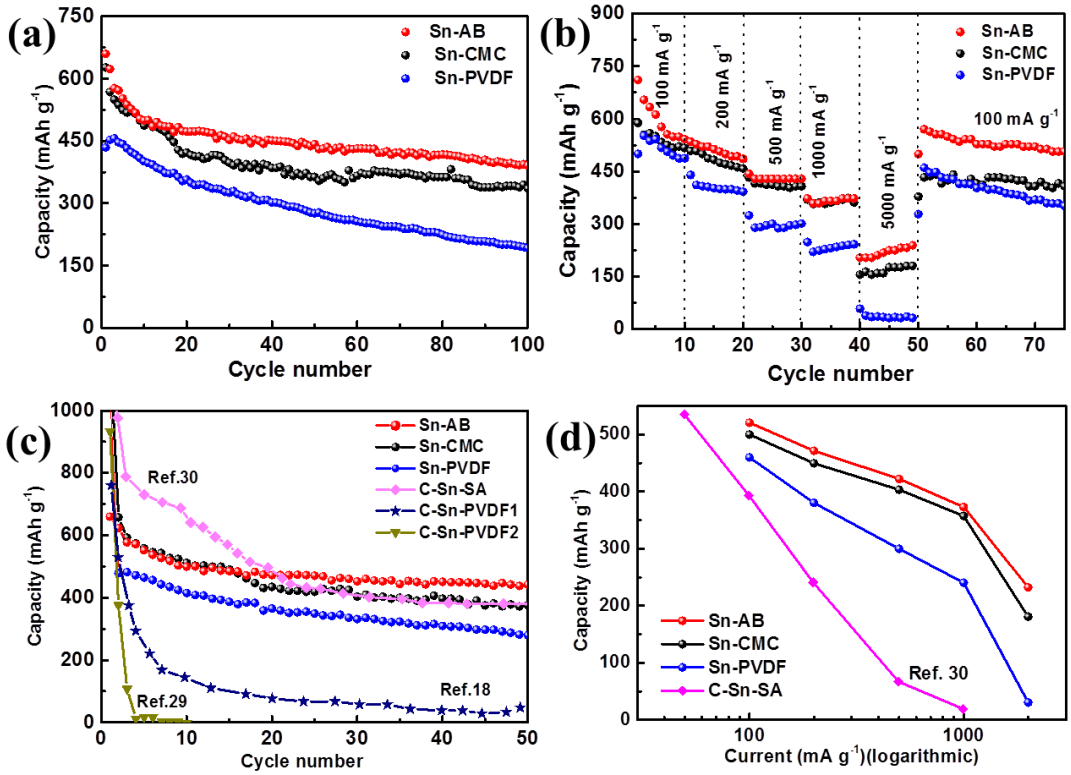

Sn-PVDF. (b) Cycling performance of Sn-AB, Sn-CMC, Sn-PVDF, and reported commercial Sn nanoparticles with PVDF binder (C-Sn-PVDF), and reported commercial Sn nanoparticles with sodium alginate binder (C-Sn-SA) at a current density of 0.1 A g^{-1}. (c) Rate capability of Sn-AB, Sn-CMC, and Sn-PVDF at various current densities. (d) Comparison of rate capability of Sn-AB, Sn-CMC, Sn-PVDF, and C-Sn-SA (Capacity vs. applied current, logarithmic).

demonstrates comparable cycling performance with the optimized sodium alginate binder for commercial tin nanoparticles electrode (C-Sn-SA).[131] Except proving the superiority of AB binder, those results also indicate the small size of Sn nanoparticles (~ 3 nm) in this work are able to enhance ion accessibility, shorten Li

ions transport path and accelerate Li ions reaction rate compared to larger commercial Sn nanoparticles (50-100 nm). Figure 4.6d shows capacity as a function of current for different Sn electrodes samples. Sn-AB displays a similar capacity decrease trend to Sn-CMC but with higher capacity all the way. On the contrary, Sn-PVDF suffers rapid capacity decay with much lower capacity. It is clear that even the worst Sn-PVDF electrode in this work can outperform the rate capability of the best reported C-Sn-SA. All of these results confirm that both the nanosized Sn and the enhanced electrode integration via applying AB binder can effectively improve the electrochemical performance of the Sn anode.

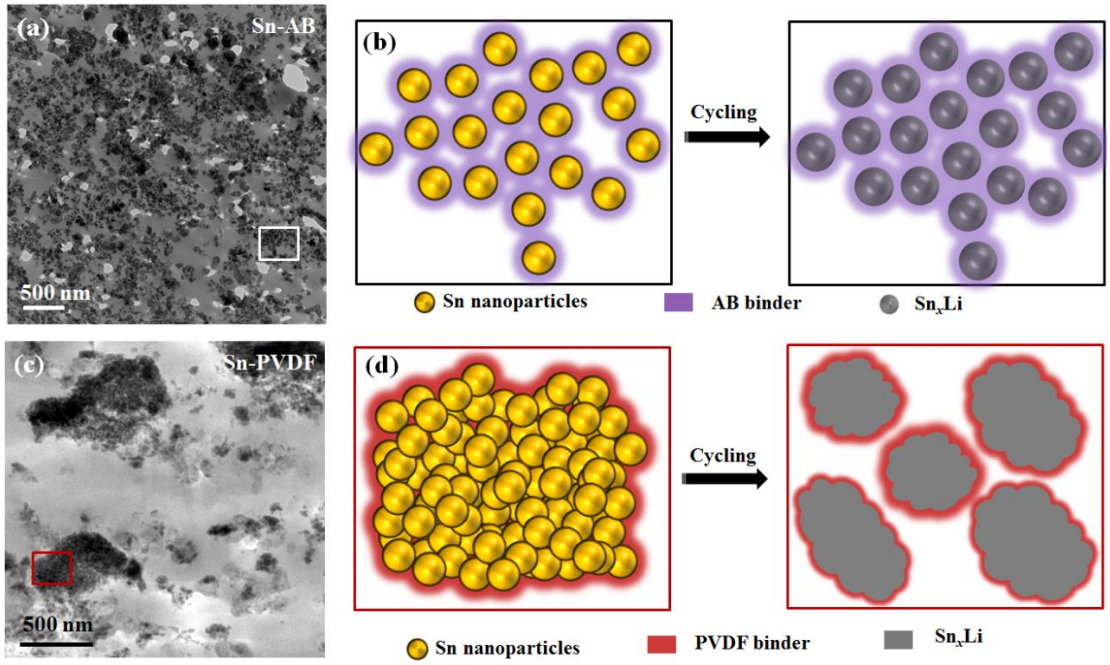

Figure 4.7 Cross-sectional TEM images obtained by ultra-thin (50 nm) microtoming method for (a) Sn-AB and (c) Sn-PVDF; Schematics of morphological changes of the electrode during the lithiation and delithiation process for (b) Sn-AB and (d) Sn-PVDF.

Cross-sectional TEM images of the three electrodes are displayed to understand the electrode structure and performance. As shown in Figure 4.7a, it is clear that the Sn-AB electrode shows evenly dispersion of Sn nanoparticles in the AB binder. The uniformity of this electrode benefits from the initial coating of Part A on the Sn nanoparticles surface and the subsequent strong crosslinking between Part A and B.

Via the crosslinking process, chemical-bonding between Sn nanoparticle and AB binder occurs between the two components. These groups tend to chemically bond to the particle surface and to form a fixed polymeric layer, leading to an intimate and strong coating of AB binder on the active material surface. As shown in Figure 4.7b, it is reasonable that this Sn-AB electrode could deliver an excellent cycling stability due to the following advantages: (1) Ideally, each Sn nanoparticle would be chemically bonding with AB binder, which can effectively enhance the integrity of the composite electrode. (2) The *in-situ* cross-linked AB binder is able to confine the Sn nanoparticles in place with high resistance to strain, serving as tensile networks to significantly alleviate the huge stress of Sn nanoparticles during the lithiation/delithiation process. In sharp contrast, the cross-sectional image of Sn-PVDF electrode (Figure 7c) shows severe particle agglomeration, due to the weak physical adhesion between PVDF and Sn nanoparticles. During the cycling (Figure 7d), the agglomerated active materials tend to be pulverized and cracked up due to the low adhesion of PVDF binder, resulting in the peeling off of active materials from current collector and electrode failure.

Moreover, the cohesive forces of all binders are estimated via static uniaxial tensile testing on an INSTRON 5943. The preparation and testing processes of samples are illustrated in the inset (Figure 4.8a). First, the electrode slurries are pasted on stainless steels with an area of 1 cm×1cm. Specimen strips are prepared by overlapping two stainless steels and subjected to drying procedure. Second, the two ends of a specimen strip are secured on computer-controlled movable stage. The tensile strength and strain to failure can be plotted as shown in Figure 4.8a. Sn-CMC showed higher tensile strength (~118.4 MPa) than Sn-PVdF (~36.8 MPa). On comparison, Sn-AB shows the highest tensile strength about 134 MPa. The strain to failure is 1, 6, and 14 % for Sn- PVdF, Sn-CMC, and Sn-AB, respectively. It is clear that the Sn-AB electrode possesses the highest toughness, which is ascribed to the exceptional adhesion property of AB binder and strong chemical bonding between AB and Sn nanoparticles, leading to high integrity of the electrode. The high toughness of AB binder, therefore, is favourable to alleviate the rupture/cracking of electrode surface and to tolerate large volume variations and serious mechanical

stress in the Sn nanoparticles. To further elucidate the superiority of AB binder, the surface morphological changes of all the electrodes after 100 cycles were investigated by SEM. As shown in Figure 4.8b, c and d, the Sn-AB electrode manifests slight surface rupturing with only very minor cracks; the cracking phenomenon of Sn-CMC shows obvious, inter-connected cracks with bigger fractures; and the Sn-PVDF not only demonstrates obvious, inter-connected cracks but loses structural integrity – one piece is peeled off from the Cu foil.

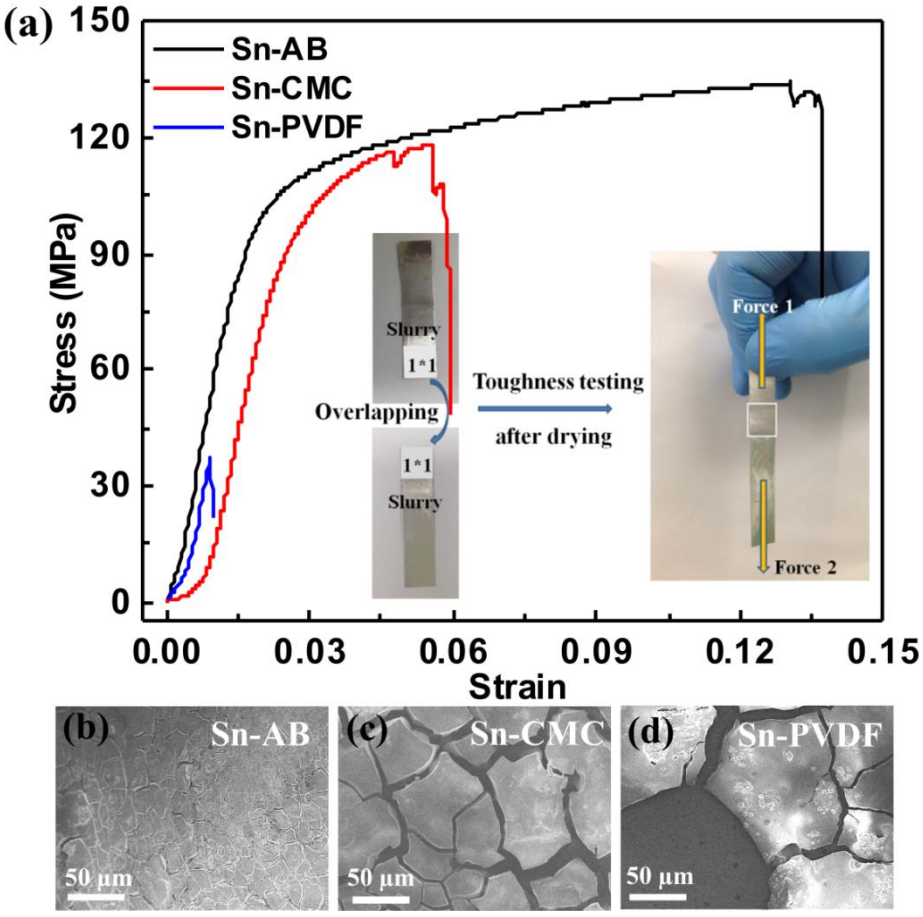

Figure 4.8 (a) Force-extension curves for all binders at a test speed of 2 mm s^{-1}; and the toughness testing processes are inserted. Morphological changes of (b) Sn-AB, (c) Sn-CMC, (d) Sn-PVDF after 100 cycles at 100 mA g^{-1}.

Furthermore, when the three electrodes were compared before and after cycling under high magnification, the structural integrity of Sn-AB was well preserved after 100 cycles (Figure 4.9b and c), showing no obvious changes from the pristine electrode (Figure 4.9a). In contrast, after 100 charge/discharge processes, slight cracking could be found for the Sn-CMC electrode (Figure 4.10); serious pulverization and cracking is observed in the Sn-PVDF electrode (Figure 4.11). These morphological variations clearly prove that the Sn-AB electrode possesses high tolerance for the drastic stress during the cycling measurement, since the binder can form a multidimensional, high-strength polymer network around Sn nanoparticles. To sum up, the enhanced electrochemical performance of Sn-AB is contributed by the following merits: the ultra-small size of the Sn nanoparticles can significantly reduce the mechanical strain generated during the charge/discharge process, thereby obstructing the fracturing of the Sn nanoparticles in all the binders.

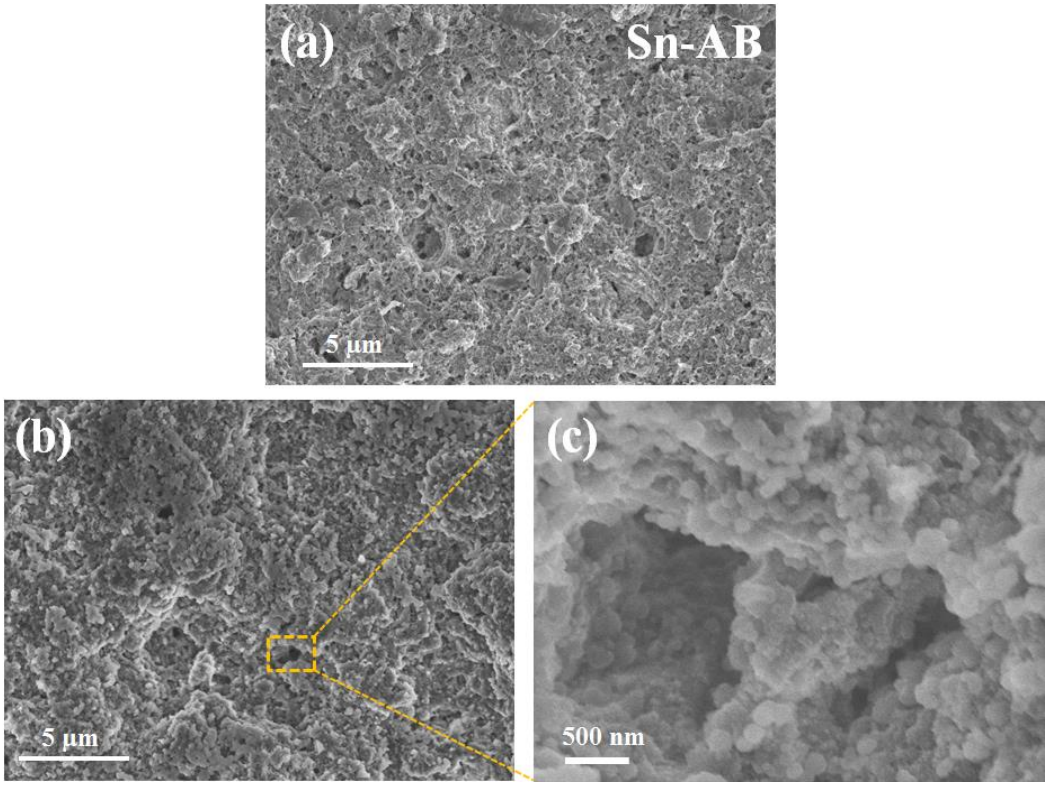

Figure 4.9 Morphological preservation of Sn-AB electrode for (a) pristine state, and after 100 cycles (b) at low magnification and (c) at high magnification.

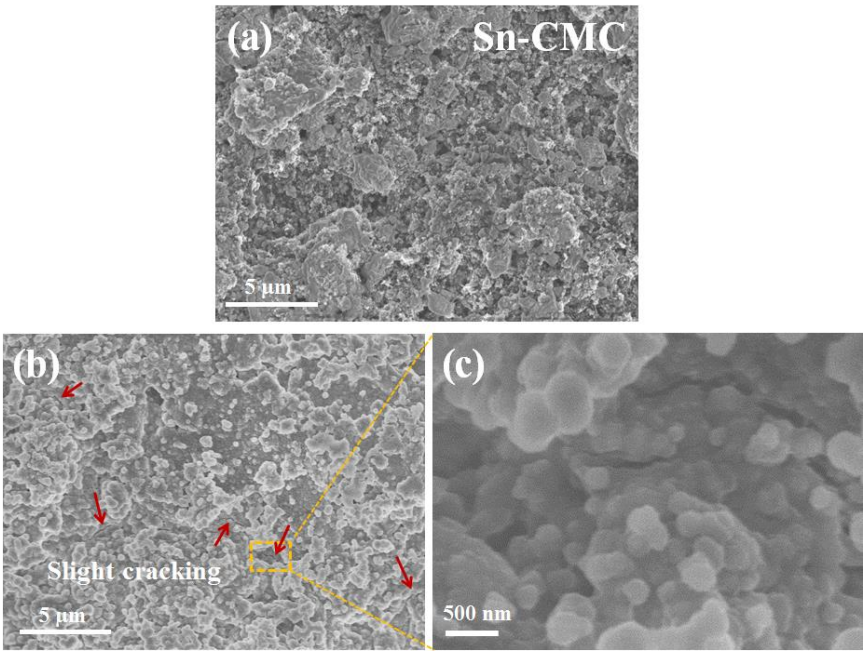

Figure 4.10 Morphological changes of Sn-CMC electrode for (a) pristine state, and after 100 cycles (b) at low magnification and (c) at high magnification.

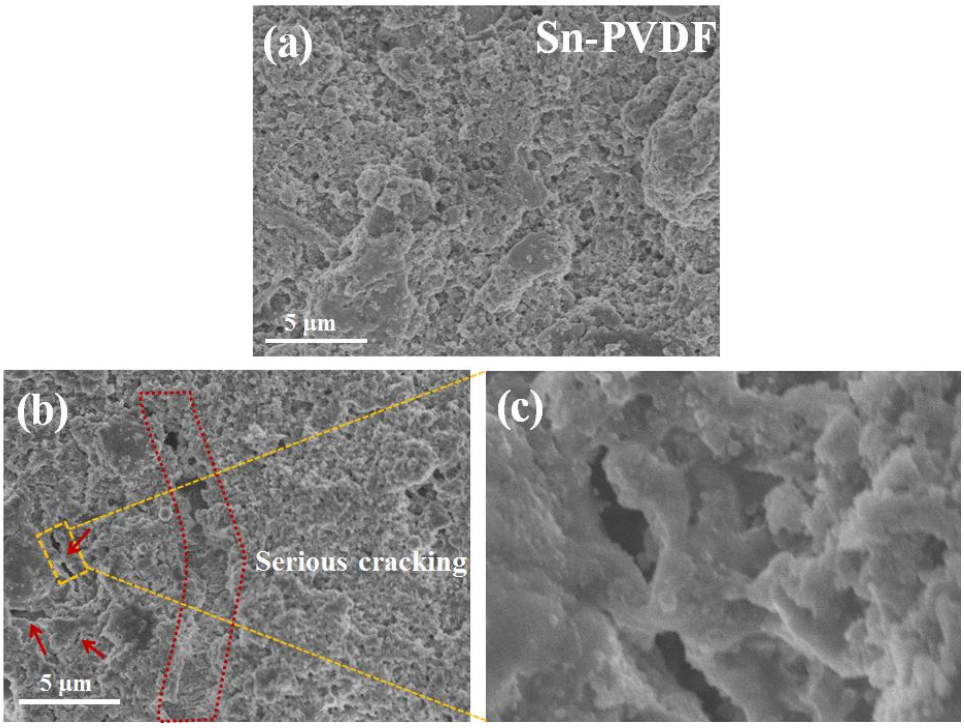

Figure 4.11 Morphological changes of Sn-PVDF electrode for (a) pristine state, and after 100 cycles (b) at low magnification and (c) at high magnification.

On the other hand, the ultrafine Sn nanoparticles can lead to fast electron transport and high ion accessibility as well. Thus, high reversible capacity and outstanding rate capability can be achieved. Significantly, the cross-linking reaction after mixing parts A and B to create the AB binder assists in building an integrated electrode, where Sn nanoparticles and active carbon are strongly bound together with intimate contact. The high-toughness Sn-AB electrode with a strong chemical binding force is capable of relieving the stress generated during expansion/contraction of Sn nanoparticles and hindering the formation and propagation of electrode cracks, leading to preservation of the electrode structure and good cycling stability with high capacity retention.

4.5 Conclusions

In summary, with the *in-situ* cross-linking reaction of the applied epoxy resin (A) and amine (B) binder, an integrated Sn nanoparticles anode has been successfully fabricated. Surprisingly, the Sn-AB electrode is superior in terms of both cycling performance and rate capability, delivering a stable capacity of 400 mA h g^{-1} over 100 cycles and superior rate capability, especially for fast charge/discharge processes (235 mA h g^{-1} at 5 A g^{-1}). Moreover, the original morphology and integration of the Sn-AB electrode surface can be well maintained after 100 cycles, due to the excellent adhesion property of AB binder and the strong chemical bonding between Sn nanoparticles and AB binder. The enhanced Li-storage properties of the Sn nanoparticles are prime benefits of the using AB binder. For this reason, the AB binder is expected to be deployed with other electrode candidates with large volume variations during cycling, and its compatibility will be explored in our future work.

CHAPTER 5 FACILE SELF-GROWTH CORE-SHELL SN@SNO2/GRAPHENE HYBIRD AS A HIGH-PERFORMANCE ANODE FOR LITHIUM ION BATTERY

A core-shell $Sn@SnO_2$ grafted graphene nanocomposite ($Sn@SnO_2/G$) was successfully fabricated by simultaneous reduction of ultrafine SnO_2 nanoparticles and carbonization of oleic acid (OA) ligands via facile low-temperature heat treatment (500 ^oC). The developed strategy offers an ingenious method to prepare elaborate $Sn@SnO_2/G$ via one-step heat-treatment. Moreover, it also can be used to prepare green graphene nanosheets via etching away the interior $Sn@SnO_2$. When applied as anodes in lithium-ion batteries, the obtained $Sn@SnO_2/G$ impressively delivers a sustainable capacity of ~ 600 mA h g^{-1} over 100 cycles. In contrast to the SnO_2/RGO, the $Sn@SnO_2/G$ electrode exhibits much better rate capability. At a medium current rate (500 mA g^{-1}), the $Sn@SnO_2/G$ and SnO_2/RGO delivered comparable reversible capacity of 470 and 422 mA h g^{-1} over 15 cycles, respectively. Surprisingly, the $Sn@SnO_2/G$ is capable of achieving a much higher capacity of 167 mA h g^{-1} at a very high rate of 5 A g^{-1}.

5.1 Introduction

Various emerging energy storage systems,[132] including lithium-air battery,[133, 134] lithium-sulphur battery,[135, 136] sodium-storage technology,[137-139] and vanadium redox battery,[140, 141] are currently attracting most of attention to power our future society. As the mainstays of portable electronic devices and electric vehicles, the pursuit on rechargeable lithium-ion batteries with high power and energy density is still urgently required.[142, 143]

Metallic Sn and tin oxide (SnO_2) have been extensively investigated due to their high theoretical capacities (993 mA h g^{-1} and 750 mA h g^{-1}).[144-147] SnO_2 is able to realize Li-storage via an irreversible/partially reversible conversion reaction during first discharge process, followed by reversible reaction between $Li_{4.4}Sn$ and Sn for the subsequent cycles. Unavoidably, the irreversibility in initial discharge process leads to low Coulombic efficiency (ICE); the intrinsic low ICE eliminates the feasibility of SnO_2 alone as anode for practical application; while it is believed that the resulted Li_2O nano-matrix during first discharge process is favorable to enhance the cycling stability of this electrode.[145, 148-150] In contrast, the Sn anode which shows high electronic conductivity and moderate operating voltage, is able to deliver good rate capability, hinder the formation of Li dendrite and improve the safety properties of LIBs.[146, 151-153] Tin-based anode, Nexelion, has been commercialized by Sony, which has proven the great potential of Sn as an appealing and competitive alternative anode to substitute the commercial graphitic anode (372 mA h g-1).[154] A large volume expansion (~300 %) of Sn, however, causes serious pulverization and severe aggregation of Sn nanoparticles during charge/discharge processes. [146, 151-153] Subsequently, active materials would electrically disconnect from the current collector, thereby resulting in inferior cycling stability and rapid capacity loss. This problem has been a major challenge in the commercialization of Sn-based anodes.

To overcome this drawback, various of studies on Sn-based /C nanocomposites have been extensively explored.[137, 152, 155-157] Nanostructured Sn-based/graphene composite stands out due to the significant enhancement on its electrochemical performance in term of cycling stability and rate capability. The nanoscaled active materials are able

to facilitate the absorption of electrolyte, the transport of electrons, and the reaction with Li ions. On the other hand, a graphene matrix, with superior properties such as high electrical conductivity and specific surface areas, could effectively enhance the electrical conductivity of the electrode, synergistically accelerating the transfer of electrons and Li ions as well. More importantly, the nanostructured architecture with free space between active materials and graphene matrix can accommodate the huge volume expansion, thereby diminishing the local mechanical stress of the collective electrode over cycling. Typically, the synthesis of Sn-graphene nanocomposite is multistep and time-consuming, is attained by partial reduction of SnO_2-graphene composite processor via heat treatment at high temperatures (700-900)[158-160] under an inert atmosphere or through chemical reduction with hydrazine or $NaBH_4$.[145, 161] Moreover, it is also complicated to fabricate the SnO_2-graphene composite processor. Different approaches such as physical mixing of SnO_2 nanoparticles together with graphene sheets[162] or spray deposition[163, 164] have been applied, which usually results in the inhomogeneous dispersion of nanoparticles on the graphene matrix. The most explored strategy involves the hydro- or solvo-thermal deposition of very small SnO_2 nanoparticles (generally around 5 nm) on GO layers.[165-167] It should be pointed out that the involved graphene oxides are commonly prepared via a modified Hummers' method, which could produce a large quantity of graphene oxide but toxic gases evolved in the process. In addition, reduced graphene oxide still maintains a relatively high C/O ratio and a large number of defects. Despite the fatal weakness of GO synthesis, the architecture of above-prepared Sn-based/graphene composites is both fragile and unstable. The Sn-based nanoparticles are prone to peel off from the graphene during charge/discharge processes,[168, 169] thereby agglomeration of Sn nanoparticles and continual formation of thick solid electrolyte interphase (SEI), causing the degeneration of the nanostructure and capacity loss. Therefore, it remains a great challenge to synthesize a stable nanostructure with high-quality graphene matrix via a green and simple method, in which the Sn-based nanoparticles are supposed to be fully wrapped into graphene.

Herein, a core-shell Sn@SnO_2 grafted graphene nanocomposite (Sn@SnO_2/G) is successfully fabricated. The Sn core guarantees the high theoretical capacity of the

composite. On the other hand, the thin SnO_2 layer (~ 5 nm) could assist the composite to achieve high stability and long cycling life. More importantly, the pure graphene nanosheets can in-situ grow around the Sn-based nanoparticles without exposing any Sn-based nanoparticles out of surface. With the aid of this unique nano-architecture, the obtained Sn@SnO_2/G anode can achieve excellent lithium-storage properties in term of reversible capacity, cycling stability, and rate capability. For comparison, SnO_2/GO composite was fabricated from the mixture of ultrafine SnO_2 nanoparticles and GO dispersion; under the same heat-treatment procedure, it is interesting that the final production is SnO_2/graphene instead of Sn@SnO_2/G, implying the critical function of OA on SnO_2 reduction.

5.2 Experimental

5.2.1 Synthesis of ultrafine SnO_2 nanoparticles

0.425 g $SnCl_2 \cdot 2H_2O$ was firstly added to a mixture of 30 mL ethanol and 60 mL water with magnetic stirring , and then the appropriate volume of 1 M NaOH solution was added to adjust the solution PH to 11. After magnetic stirring of 1 h, the transparent solution was treated at 120 °C for 6 h by hydrothermal. SnO_2 nanoparticles can be obtained by washing the white participation with water and ethanol 3 times, respectively.

5.2.2 Synthesis of core-shell Sn@SnO_2/G and SnO_2/RGO

The SnO_2 nanoparticles were immersed into 30 mL oleic acid (OA) for 12 h. The obtained OA-capped SnO_2 colloidal was placed into combustion boat, followed by tightly wrapped by Al foil. It was then subjected to heat treatment at 500 °C for 2 h in an Ar atmosphere. When naturally cooled down to room temperature, the self-constructed core-shell Sn@SnO_2/G hybrid was prepared straightforward. For comparison, SnO_2/RGO was synthesis by heat treatment of the mixture SnO_2 nanoparticles and graphene oxides at the same condition.

5.2.3 Structural characterization

The morphologies of the samples were investigated by field-emission scanning electron microscopy (FESEM; JEOL JSM-7500FA) and transmission electron microscopy (TEM, JEOL 2011, 200 keV). Raman spectra were collected by a 10 mW helium/neon laser at 632.8 nm excitation, which was filtered by a neutral density filter to reduce the laser intensity and a charge-coupled detector (CCD). The XRD patterns were collected by powder X-ray diffraction (XRD; GBC MMA diffractometer) with Cu Kα radiation at a scan rate of 2° min^{-1}. The Brunauer-Emmett-Teller (BET) method was utilized to calculate the specific surface areas (SBET), using adsorption data in a relative pressure (P/P_0) range from 0.04 to 0.2. The pore volume and pore size distributions were derived from the adsorption branches of isotherms by using the Barrett-Joyner-Halenda (BJH) model. The total pore volume (Vt) was estimated from the amount adsorbed at a relative pressure P/P_0 of 0.995. The surface morphology and thickness of the graphene nanosheets were examined by atomic force microscopy (AFM) (Asylum Research MFP-3D) at room temperature.

5.2.4 Electrochemical measurements

The electrochemical tests were conducted by assembling coin-type half-cells in an argon-filled glove box. The slurries were prepared by fully mixing 80 wt. % active materials ($Sn@SnO_2$/G and SnO_2/RGO), 10 wt. % carbon black, and 10 wt. % carboxymethyl cellulose (CMC) in an appropriate amount of water solvent by planetary mixer (KK-250S). The obtained slurries were pasted on copper foil using a doctor blade with a thickness of 100 μm, which was followed by drying at 80 °C in a vacuum oven overnight. The working electrodes were prepared by punching the electrode film into discs 0.97 cm in diameter. The lithium foils were employed as both reference and counter electrode. The electrodes were separated by a glass fiber separator. The electrolyte was 1.0 M $LiPF_6$ in 3:4:3 (weight ratio) ethylene carbonate (EC) / dimethyl carbonate (DMC) / diethylene carbonate (DEC), with 5 wt. % fluoroethylene carbonate (FEC) additive from Novolyte Technologies. The electrochemical performance was tested on a LAND Battery Tester. Cyclic voltammetry and impedance testing was performed using a Biologic VMP-3 electrochemical workstation.

5.3 Characterizations of morphology and structure

Core-shell Sn@SnO_2/G nanocomposite is fabricated by simultaneous reduction of ultrafine SnO_2 nanoparticles and carbonization of oleic acid (OA) ligands via facile low-temperature heat treatment (500 °C). As illustrated in Scheme 5.1, in order to fabricate the core-shell Sn@SnO_2/G nanocomposite, two processes are evolved. First, the SnO_2-OA complex was formed via direct immersion overnight, in which each of SnO_2 nanoparticles is uniformly capped by OA liquid. Upon heating at 500 °C under Ar atmosphere, SnO_2 nanoparticles in-situ react with OA ligands, which firstly results in the formation of core-shell Sn@SnO_2 nanoparticles (~5 nm). The low melting point (231.9 °C) of Sn core and SnO_2 shell rupture render the adjacent nanoparticles re-combine into large nanoparticles, leading to the formation of core-shell Sn@SnO_2/G nanocomposite (~20-120 nm). During this process, high-quality graphene nanosheets were in-situ formed from the OA coating layer with the core-shell Sn@SnO_2 embedded inside.

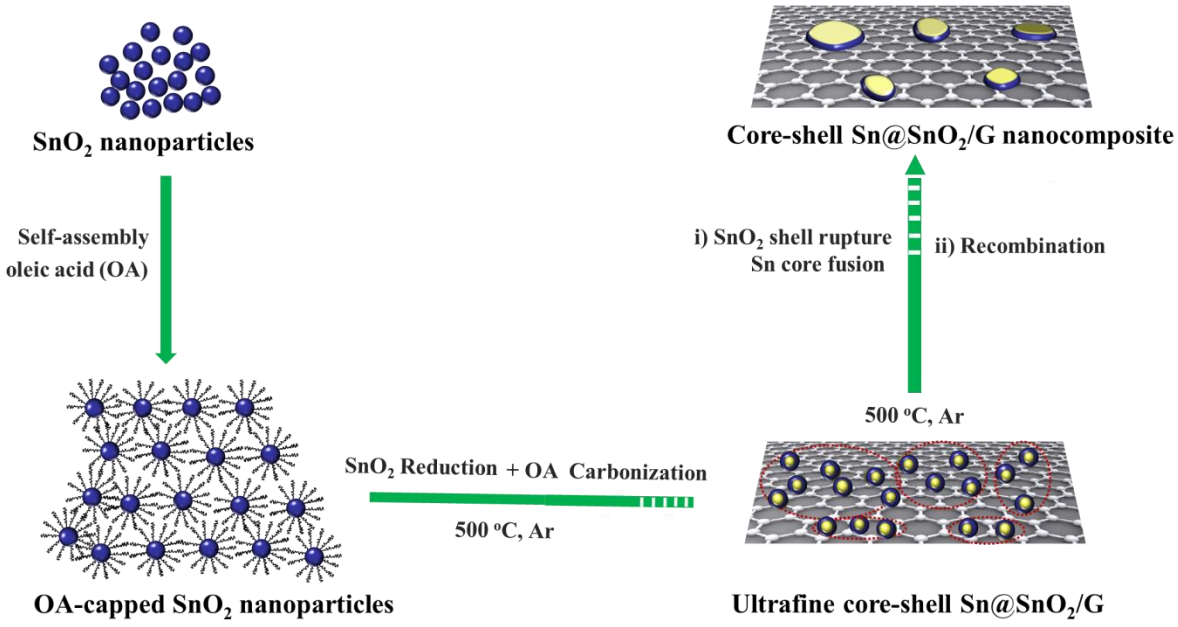

Scheme 5.1 Schematic representation of the preparation of core-shell Sn@SnO_2/G by OA assembling.

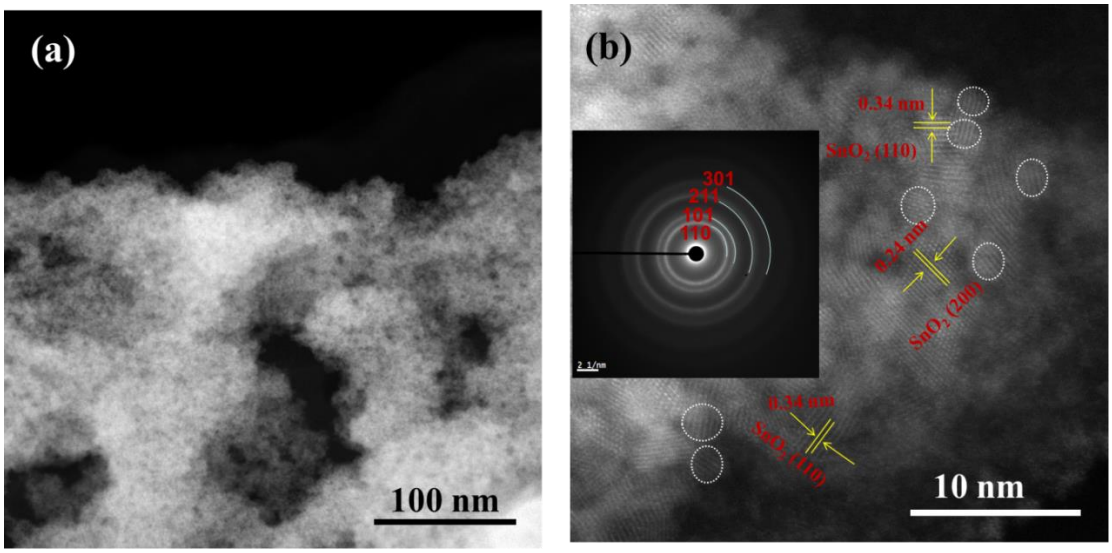

Figure 5.1 (a) Low-mag TEM and (b) HRTEM with corresponding selected area diffraction pattern (inset) of pristine SnO_2 ultrafine nanoparticles.

The morphology of the nanocomposite was observed via scanning electron microscopy (SEM) and transmission electron microscopy (TEM). As shown in Figure 5.1a, the particle size of fresh-prepared SnO_2 is ~ 5 nm with slight agglomeration with the surrounding particles; the measured lattice fringes in HRTEM and indexed selected area electron diffraction pattern (SAED) are consistent with the pure phase of SnO_2 (Figure 5.1b).

As shown in Figure 5.2a, a large amount of nanoparticles were perfectly concealed by large graphene nanosheets. The graphene nanosheets are very thin and possess platelet-like structure. For the high-magnification SEM image (Figure 5.2b), it is clear that the particle sizes vary, which is supposed to be determined by the numbers of SnO_2 nanoparticles in the vicinity. TEM image (Figure 5.2c) clearly display the particle size in the range from 20 to 120 nm, the graphene matrix shows thin transparent sheets and thick ripples, which implies that the graphene nanosheets are only a few layers and partially crumpling into wrinkled structure. As revealed in Figure 5.2d – 5.2f, it is interesting that the nanoparticles possess a core-shell structure. The high-resolution TEM image (HRTEM) reveals lattice spacings consistent with a core of crystalline Sn and the shell of SnO_2. The inner lattice

spacing of 0.2 nm corresponds to the (211) plane of Sn, and the outer lattice spacing of 0.34 nm belongs to the (110) plane of SnO_2. Moreover, the graphene matrix is revealed to be 5-10 layers with a (002) interlayer spacing of 0.37 nm. Phase mappings based on EDS principal component analyses were conducted to confirm the universality of this core-shell structure. Regardless of the sizes of nanoparticles, the core-shell structures are well-constructed and thickness of each SnO_2 shells are uniform (~ 5 nm). It is noteworthy that this unique nano-architecture, graphene encapsulated Sn-based composite via in-situ growth, is expected to be well-preserved and endure the large volume expansion.

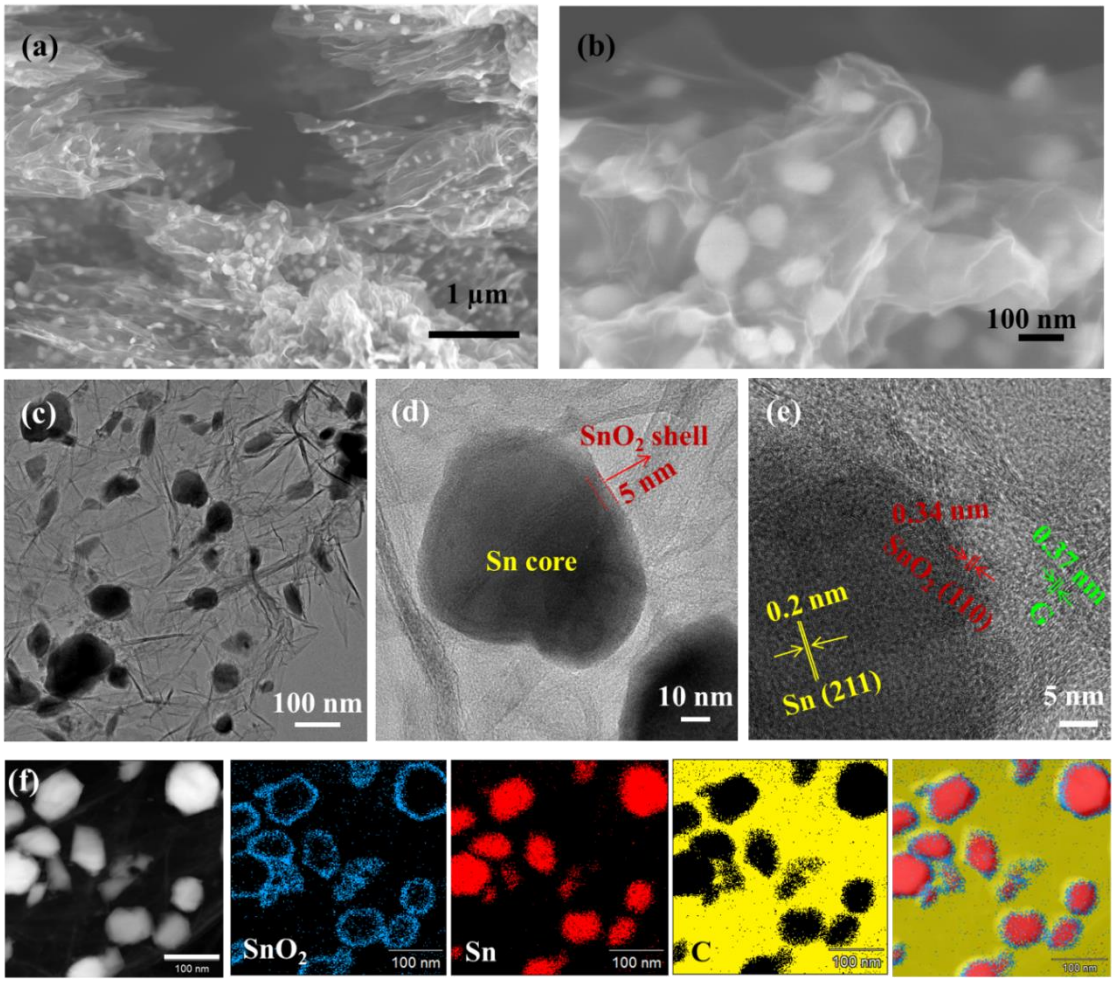

Figure 5.2 Morphological and compositional characterization of core-shell $Sn@SnO_2/G$: SEM images at (a) low and (b) high magnification; (c), (d) low magnification TEM, and (e) HRTEM images; (f) phase mappings of SnO_2, Sn, and C.

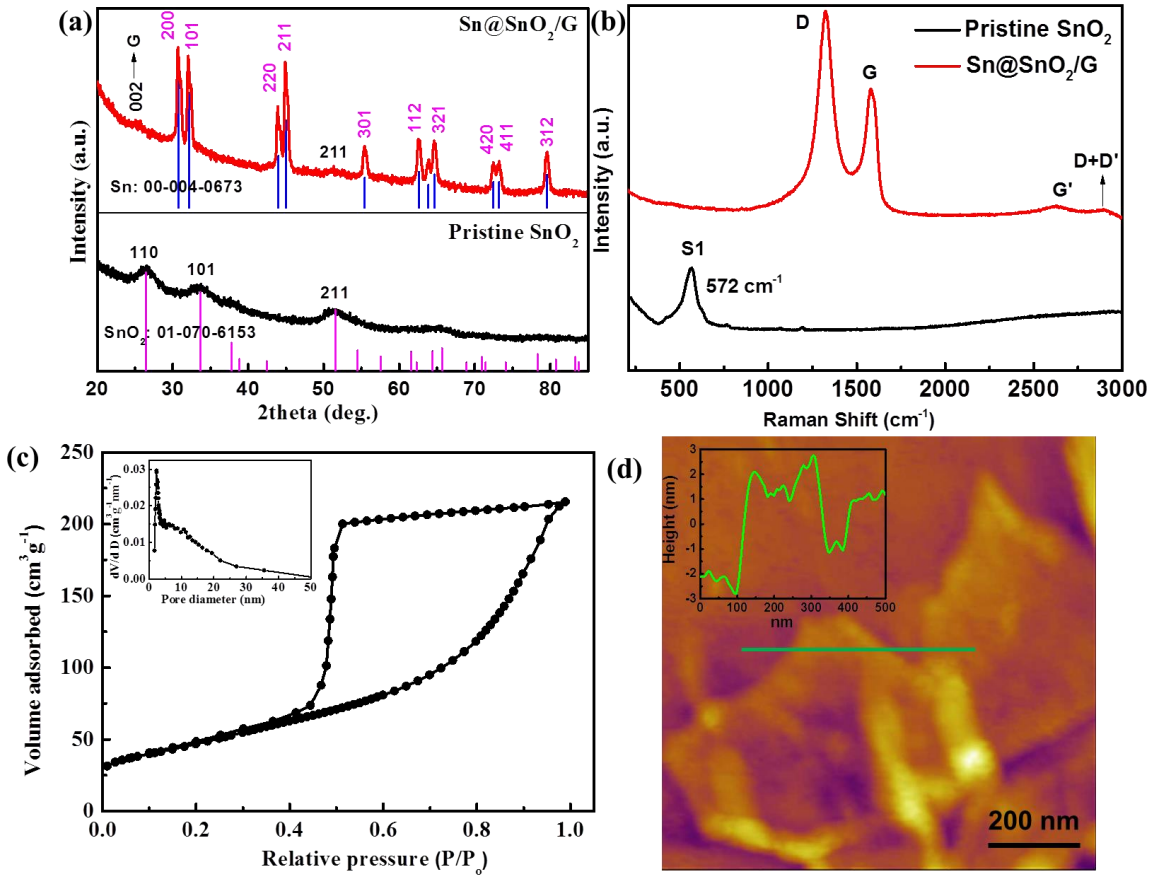

Figure 5.3 (a) XRD patterns of $Sn@SnO_2/G$ and pristine SnO_2 with the standard XRD patterns of SnO_2 and Sn (inset). (b) Raman spectrum of $Sn@SnO_2/G$ and pristine SnO_2. (c) N_2 adsorption/desorption isotherms with pore size distribution plot (inset) of $Sn@SnO_2/G$. (d) AFM image of $Sn@SnO_2/G$ with the inset profile corresponding to the green line.

The XRD patterns of $Sn@SnO_2/G$ and pristine SnO_2 has been displayed in Figure 5.3a. The weak diffraction peaks with low intensity and resolution indicate very small particle size of the obtained SnO_2. All the diffraction peaks are well indexed to a tetragonal SnO_2 phase (JCPDS no. 88-0287) without any impurity. In contrast, the diffraction peaks of $Sn@SnO_2/G$ are narrowing with high intensity, indicating a high degree of crystallization and an increase in grain size of the $Sn@SnO_2$ nanoparticles. A bump at 25.4^o is ascribed to the (002) peak of graphene matrix. A slight peak (211) of SnO_2 can be observed, which indicates the presence of SnO_2 in the hybrid. All the

other peaks can be indexed to be crystalline Sn (JCPDS no. 88-0287). As revealed in Figure 5.3b, the Raman spectrum of pristine SnO_2 features a distinct peak at 722.9 cm^{-1}, which corresponds to the disorder activation of S1.[170] This typical Raman peak implies the particle size of pristine SnO_2 is around 5 nm, in good agreement with the SEM and TEM results. The Sn@SnO_2/G hybrid displays the typical bands for graphene without the presence of S1 peak of SnO_2, including the G-band at ~1583 cm^{-1}, strong D-band at ~1327 cm^{-1}, second-order Raman overtones G' at 2634 cm^{-1}, and disorder-induced D+D' bands at ~2899 cm^{-1}. [171] The Raman spectrum, therefore, directly confirms the occurrence of SnO_2 reduction and the formation of high-quality graphene. The N_2 absorption analysis of Sn@SnO_2/G hybrid show type-IV curves in Figure 5.3c. The Brunauer-Emmett-Teller (BET) surface area and total pore volume is calculated to be as high as 169.8 m^2 g^{-1} and 0.33 cm^3 g^{-1}, respectively, which is favorable to achieve high ion/electrolyte accessibility and fast ion transportation of active materials. The quality and thickness of graphene nanosheets is further confirmed via atomic force microscope (AFM), which shows the typical flakes with multilayer structure. The thickness of two large graphene sheets is ~ 5 and 2 nm, respectively, corresponding to the stack of 5-13 graphene nanolayers. The AFM results are in good agreement with the HRTEM images in Figure 5.3d, indicating the prepared graphene nanosheets via this green and low-temperature strategy is much superior to the conventional reduced graphene oxide, which involves serious environmental pollution and requires high-temperature or strong reducing agent.

In addition, the contrast sample is prepared from the mixture of pure SnO_2 nanoparticles and graphene oxides under the same heat-treatment process. Surprisingly, the obtained nanocomposite shows totally different morphology to Sn@SnO_2/G, which anchors numbers of ultrasmall nanoparticles on the surface of graphene matrix (Figure 5.4a and 5.4b). As shown in Figure 5.4c, it is interesting that there is no Sn formed when heat up the mixture of SnO_2 and RGO by the same temperature, which proves the superiority of this method for the synthesis of Sn metal and high-quality graphene matrix.

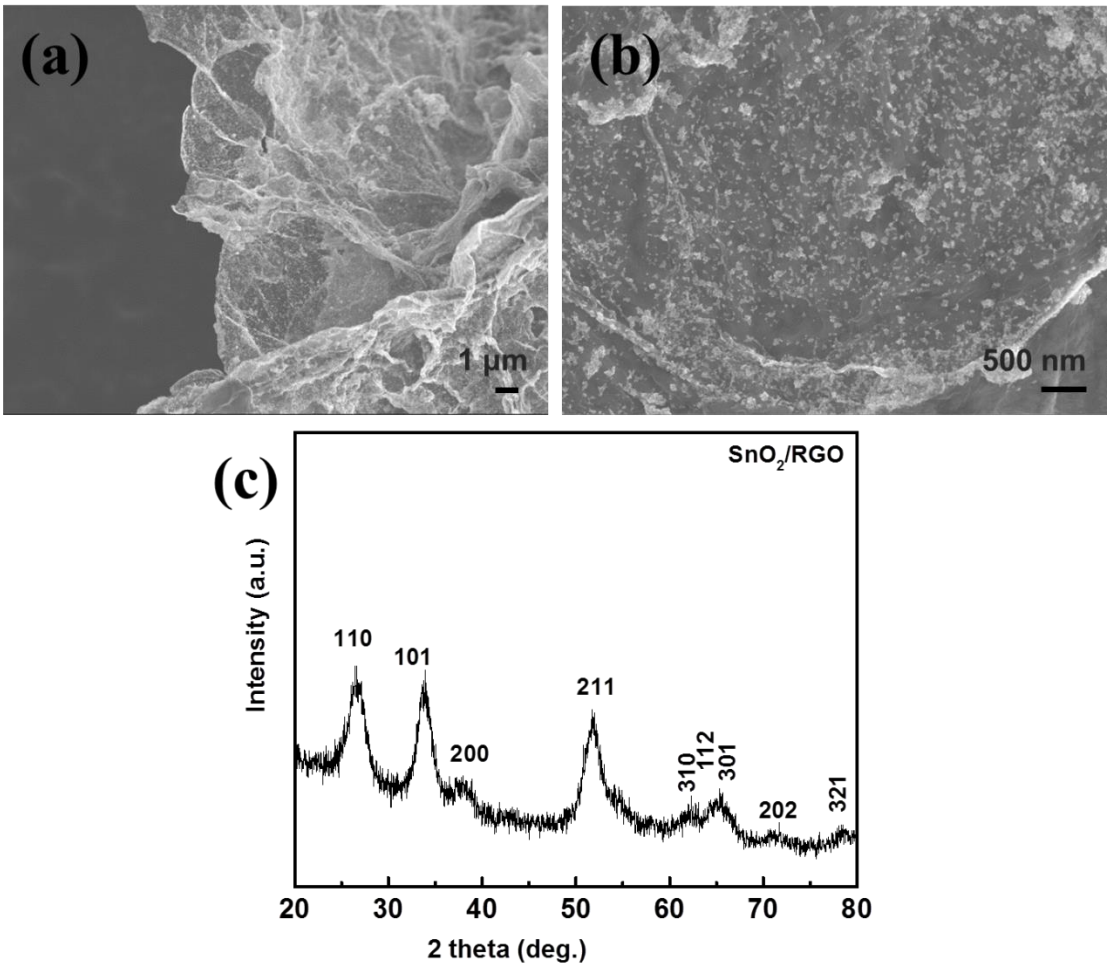

Figure 5.4 The SEM images of SnO_2/RGO at (a) low and (b) high magnification.

5.4 Electrochemical performance

The electrochemical performance of Sn@SnO_2/G composite was evaluated as anode in lithium ion batteries. For comparison, the SnO_2/RGO was also tested. Figure 5.5a and b show the cyclic voltammetry curves (CV) of Sn@SnO_2/G and SnO_2/RGO in the range between 0.005 and 2.5 V. For the first cathodic sweep, two irreversible peaks evolve at approximately 0.72 and 0.066 V, which are ascribed to the SnO_2 reduction and SEI formation and to the alloying process of Sn, respectively. Subsequent cycles show high repetition with three well defined peaks at 0.935, 0.37 and 0.24 V. The peak observed at 0.935 V is associated with the reduction of SnO_2 to Sn. The peaks recorded at 0.37 and 0.24 V are attributed to the alloying

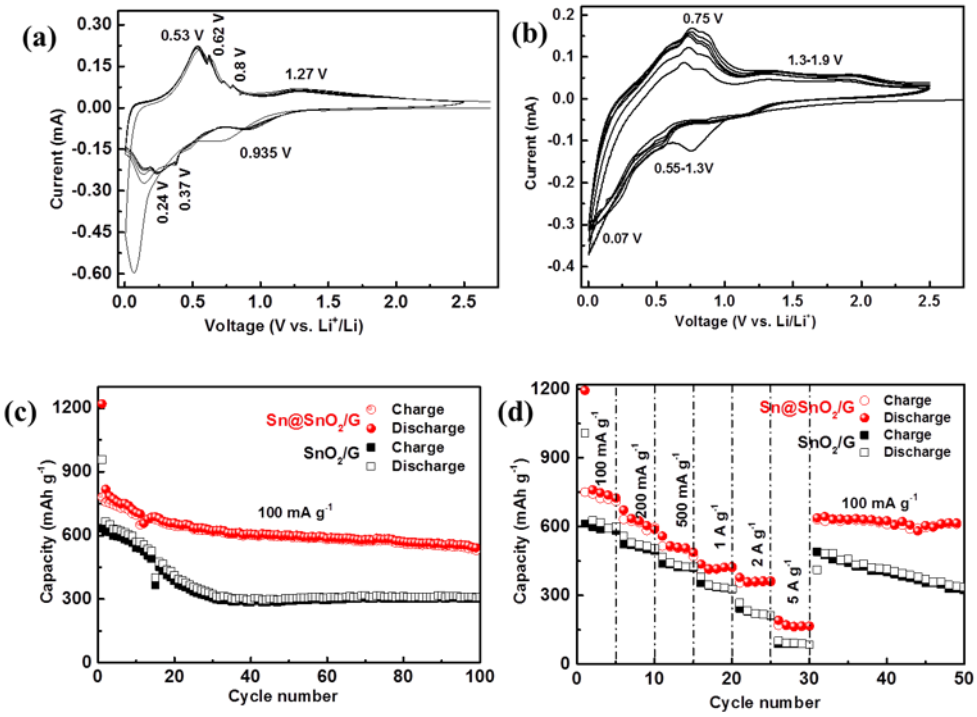

Figure 5.5 Cycling voltammograms of (a) Sn@SnO_2/G and (b) SnO_2/RGO. (c) Cycling performance, and (d) rate capability of Sn@SnO_2/G and SnO_2/RGO

process into Li_xSn of Sn. All the anodic curves show four peaks centered at 0.53, 0.62, 0.8 and 1.27 V. The three low-voltage peaks (under 0.9 V) correspond to the

dealloying process from Li_xSn to Sn. The high-voltage peak at 1.27 V belongs to the reversible redox reaction of Sn into SnO_2. The high repetition of CV curves indicates the excellent cycling stability of this hybrid. In agreement with the typical CV peaks, SnO_2/G shows reversible cathodic peaks at 0.55 -1.3 V and anodic peaks at 1.3- 1.9 V, which are ascribed to the initial reduction of SnO_2 to Sn and partially reversible formation of SnO_2, respectively. Another pair of reversible peaks at 0.07 and 0.75 V corresponds to the alloying and dealloying processes between Sn and SnxLi.[172] The current becomes more intensive for the following scan, indicating low lithium electroactivity of SnO_2/RGO composite. As expected, the Sn@SnO_2/G composite in Figure 5.5c is able to remain high capacity retention of ~ 69 % after 100 cycles. It delivers an initial reversible capacity of 781 mA h g^{-1} and undergoes gradually capacity decay to 645 mA h g^{-1} over 20 cycles. It is impressive that the capacity of Sn@SnO_2/G composite is stabilized at ~ 600 mA h g^{-1} over 100 cycles. In contrast, SnO_2@RGO exhibits much inferior electrochemical properties, which suffers rapid capacity decay to ~310 mA h g^{-1} after 30 cycles and only maintains a capacity of ~180 mA h g^{-1} over 100 cycles. As shown in Figure 5.5d, the prevailing of Sn@SnO_2/G is further underscored by its superior rate capability. At a medium current rate (500 mA g^{-1}), the Sn@SnO_2/G and SnO_2/RGO delivered comparable reversible capacity of 470 and 422 mA h g^{-1} over 15 cycles, respectively. Surprisingly, the Sn@SnO_2/G is capable of achieving a much higher capacity of 167 mA h g^{-1} at a very high rate of 5 A g^{-1}, only remaining a reversible capacity of 85 mA h g^{-1} for the SnO_2/RGO electrode.

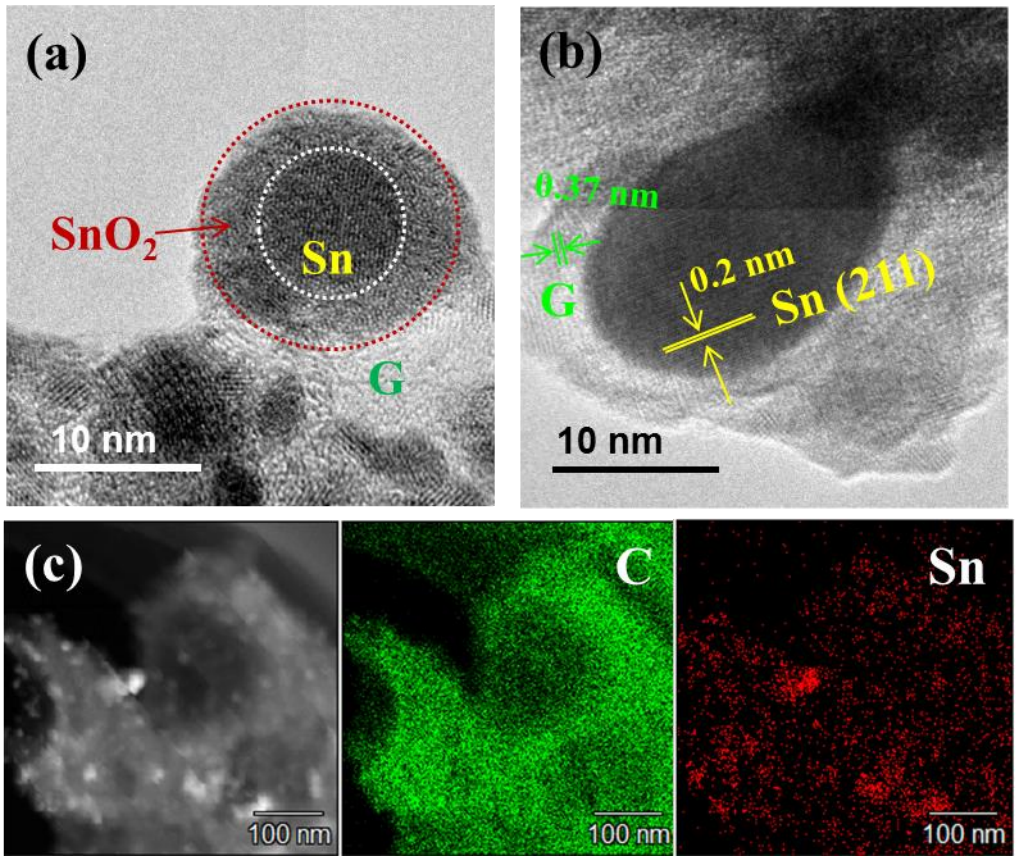

Figure 5.6 HRTEM image of $Sn@SnO_2/G$ of (a) before and (b) after rate-capability test. (c) Elemental mappings of C and Sn for the electrode after rate-capability test.

The morphological and compositional changes of $Sn@SnO_2/G$ after rate-capability test have been investigated via TEM in Figure 5.6. Consistent with the results in Figure 5.2f, the pristine $Sn@SnO_2/G$ particles display the well-constructed nano-architecture with $Sn@SnO_2$ embedded in graphene matrix (Figure 5.6a). As illustrated in Figure 5.6b, the electrode retains the particle morphology with fringe lattice of ~0.2 nm, which corresponds to the (211) phase of metallic Sn. The structure of G matrix is also well maintained. It is noteworthy that the SnO_2 shell is hard to be observed, which is due to that the oxidation from Sn to SnO_2 is likely to be partially reversible or irreversible. The elemental mappings of C and Sn show that the morphology of active material embedded in graphene matrix could be well preserved without agglomeration and pulverization of active materials, thereby resulting in excellent cycling stability and enhanced capacity.

The outstanding electrochemical performance of $Sn@SnO_2$/G hybrid in terms of specific capacity and cycling stability could be ascribed to the following factors: First, the high ratio of Sn in the composite leads to high overall capacity of the electrode due to theoretical capacity of Sn itself. Second, the thin SnO_2 shell is not only able to contribute to the capacity, but also favorable for improving the cycling stability based on the initial conversion mechanism. Therefore, the unique core-shell $Sn@SnO_2$ nanocomposite can essentially serve as a potential anode material, which could offer high capacity and stable cycling life as well. Moreover, the in-situ growth of graphene matrix accounts for the great improvement of $Sn@SnO_2$/G hybrid, which could fully seal the core-shell $Sn@SnO_2$ inside, thereby preventing the active material from pulverization and realizing the nanostructure preservation and electrode integrity.

5.5 Conclusions

In summary, with the aid of OA ligands, a composite with core-shell $Sn@SnO_2$ fully wrapped by graphene nanosheets were successfully synthesized via a facile low-temperature heat treatment. This strategy explored a novel and green approach to simultaneously fabricate unique core-shell $Sn@SnO_2$ and high-quality graphene nanosheets. Applied as anode in LIBs, the constructed nanostructure endowed the $Sn@SnO_2$/G composite with enhanced capacity, excellent cycling stability, and superior rate capability. The finding offers an ingenious method to prepare green graphene nanosheets via etching away the interior $Sn@SnO_2$ as well.

CHAPTER 6 CONCLUSIONS

In this Master's study, Sn-based materials, including ultrafine Sn nanoparticles and Sn@SnO_2-G nanocomposite, were synthesized and investigated as promising anode materials in rechargeable lithium-ion batteries. Furthermore, a new type of commercial AB glue was examined as functional binder in Sn nanoparticles anode for rechargeable lithium-ion batteries.

Tin based materials have been recognized as the most promising alternative to replace graphitic carbon for lithium ion battery anodes. Systematic investigation, including material preparation and binder invention, has been involved in this study. When commercial AB glue is developed as a new binder, the ultrafine Sn nanoparticles could deliver the best performance than conventional CMC and PVDF binder. The results indicate that the binder, which tends to be neglected in research, plays a key role in performance enhancement for active material, especially for that with huge volume variations during charge/discharge processes. With the *in-situ* cross-linking reaction of the applied epoxy resin (A) and amine (B) binder, this high-adhesive AB binder could guarantee the high integrity of the constructed electrode, retaining the original morphology and integration of the Sn-AB electrode even after 100 cycles.

Moreover, an elaborate Sn@SnO_2/G architecture has been constructed. The interior Sn core results in the high theoretical capacity of the composite. The thin SnO_2 layer (~ 5 nm) is favourable to enhance cycling stability for the composite. More importantly, the pure graphene nanosheets, in-situ grown around the Sn-based nanoparticles, could fully wrap Sn-based nanoparticles inside, thereby forming favourable SEI film and ensuring the morphology preservation of active materials. With the aid of this unique nano-architecture, the Sn@SnO_2/G anode can achieve excellent lithium-storage properties in terms of reversible capacity, cycling stability, and rate capability.

In summary, the research offers a reference for the practical application of Sn-based electrode materials in LIBs, and is expected to promote its advancement of electrochemical performance and technology. The synthetic methods for preparation of ultrafine Sn nanoparticles and Sn@SnO_2/G nanocomposite include: hydrothermal,

room-temperature precipitation, and low-temperature heat treatment. All involved methods are easy to achieve, and suitable for large-scale application, thus hold great promise for industry commercialization. It is still challengeable to commercialize these Sn-based anodes at the current stage. Significantly, more efforts are supposed to be made on improving the initial Coulombic efficiency of both Sn-based anodes, and the experimental results of full cells paired with commercialized graphite are essential and imperative.

REFERENCES

1. Etacheri, V.; Marom, R.; Elazari, R.; Salitra, G.; Aurbach, D. *Energy & Environmental Science* **2011,** 4, (9), 3243-3262.
2. Armand, M.; Tarascon, J.-M. *Nature* **2008,** 451, (7179), 652-657.
3. Wu, H. B.; Chen, J. S.; Hng, H. H.; Lou, X. W. D. *Nanoscale* **2012,** 4, (8), 2526-2542.
4. Tarascon, J.-M.; Armand, M. *Nature* **2001,** 414, (6861), 359-367.
5. Zhan, F.; Jiang, L.; Wu, B.; Xia, Z.; Wei, X.; Qin, G. *Journal of Alloys and Compounds* **1999,** 293, 804-808.
6. Ikeda, H.; Saito, T.; Tamura, H. In *Manganese dioxide as Cathodes for Lithium Batteries*, Manganese Dioxide Symp.,[Proc.], 1975; pp. 384-401.
7. Van Gool, W. *Journal of Solid State Chemistry* **1973,** 7, (1), 55-58.
8. Whittingham, M. S. *Science* **1976,** 192, (4244), 1126-1127.
9. Mizushima, K.; Jones, P.; Wiseman, P.; Goodenough, J. *Materials Research Bulletin* **1980,** 15, (6), 783-789.
10. Murphy, D.; Di Salvo, F.; Carides, J.; Waszczak, J. *Materials Research Bulletin* **1978,** 13, (12), 1395-1402.
11. Lazzari, M.; Scrosati, B. *Journal of The Electrochemical Society* **1980,** 127, (3), 773-774.
12. Nagaura, T.; Tozawa, K. *Prog. Batteries Solar Cells* **1990,** 9, 209.
13. Geim, A. K.; Novoselov, K. S. *Nature Materials* **2007,** 6, (3), 183-191.
14. Yoshino, A. *Angewandte Chemie, International Edition* **2012,** 51, (24), 5798-5800.
15. Nitta, N.; Wu, F.; Lee, J. T.; Yushin, G. *Materials Today* **2015,** 18, (5), 252-264.
16. Du Pasquier, A.; Plitz, I.; Menocal, S.; Amatucci, G. *Journal of Power Sources* **2003,** 115, (1), 171-178.
17. Ellis, B. L.; Lee, K. T.; Nazar, L. F. *Chemistry of Materials* **2010,** 22, (3), 691-714.
18. Dahn, J.; von Sacken, U.; Michal, C. *Solid State Ionics* **1990,** 44, (1), 87-97.
19. Thongtem, T.; Thongtem, S. *Inorganic Materials* **2006,** 42, (2), 202-209.
20. Rougier, A.; Gravereau, P.; Delmas, C. *Journal of The Electrochemical Society* **1996,** 143, (4), 1168-1175.
21. Shi, X.; Wang, C.; Ma, X.; Sun, J. *Materials Chemistry and Physics* **2009,** 113, (2), 780-783.
22. Li, D.; Peng, Z.; Ren, H.; Guo, W.; Zhou, Y. *Materials Chemistry and Physics* **2008,** 107, (1), 171-176.
23. Sakamoto, K.; Hirayama, M.; Sonoyama, N.; Mori, D.; Yamada, A.; Tamura, K.; Mizuki, J. i.; Kanno, R. *Chemistry of Materials* **2009,** 21, (13), 2632-2640.
24. Pouillerie, C.; Croguennec, L.; Biensan, P.; Willmann, P.; Delmas, C. *Journal of The Electrochemical Society* **2000,** 147, (6), 2061-2069.
25. Arai, H.; Okada, S.; Sakurai, Y.; Yamaki, J.-i. *Solid State Ionics* **1998,** 109, (3), 295-302.
26. Naghash, A.; Lee, J. Y. *Electrochimica Acta* **2001,** 46, (15), 2293-2304.
27. Park, S. H.; Sun, Y.-K.; Park, K. S.; Nahm, K. S.; Lee, Y. S.; Yoshio, M. *Electrochimica Acta* **2002,** 47, (11), 1721-1726.
28. Gu, M.; Belharouak, I.; Zheng, J.; Wu, H.; Xiao, J.; Genc, A.; Amine, K.; Thevuthasan, S.; Baer, D. R.; Zhang, J.-G. *ACS Nano* **2012,** 7, (1), 760-767.

29. Tu, J.; Zhao, X.; Cao, G.; Zhuang, D.; Zhu, T.; Tu, J. *Electrochimica Acta* **2006,** 51, (28), 6456-6462.
30. Yabuuchi, N.; Ohzuku, T. *Journal of Power Sources* **2003,** 119, 171-174.
31. Stewart, S. G.; Srinivasan, V.; Newman, J. *Journal of The Electrochemical Society* **2008,** 155, (9), A664-A671.
32. Martha, S.; Markevich, E.; Burgel, V.; Salitra, G.; Zinigrad, E.; Markovsky, B.; Sclar, H.; Pramovich, Z.; Heik, O.; Aurbach, D. *Journal of Power Sources* **2009,** 189, (1), 288-296.
33. Martha, S. K.; Sclar, H.; Framowitz, Z. S.; Kovacheva, D.; Saliyski, N.; Gofer, Y.; Sharon, P.; Golik, E.; Markovsky, B.; Aurbach, D. *Journal of Power Sources* **2009,** 189, (1), 248-255.
34. Liu, Q.; Mao, D.; Chang, C.; Huang, F. *Journal of Power Sources* **2007,** 173, (1), 538-544.
35. Molenda, J.; Ziemnicki, M.; Marzec, J.; Zając, W.; Molenda, M.; Bućko, M. *Journal of Power Sources* **2007,** 173, (2), 707-711.
36. Thackeray, M.; De Picciotto, L.; De Kock, A.; Johnson, P.; Nicholas, V.; Adendorff, K. *Journal of Power Sources* **1987,** 21, (1), 1-8.
37. Thackeray, M. M. *Journal of the American Ceramic Society* **1999,** 82, (12), 3347-3354.
38. Kim, D. K.; Muralidharan, P.; Lee, H.-W.; Ruffo, R.; Yang, Y.; Chan, C. K.; Peng, H.; Huggins, R. A.; Cui, Y. *Nano Letters* **2008,** 8, (11), 3948-3952.
39. Hosono, E.; Kudo, T.; Honma, I.; Matsuda, H.; Zhou, H. *Nano Letters* **2009,** 9, (3), 1045-1051.
40. Yang, Y.; Xie, C.; Ruffo, R.; Peng, H.; Kim, D. K.; Cui, Y. *Nano Letters* **2009,** 9, (12), 4109-4114.
41. Lee, H.-W.; Muralidharan, P.; Ruffo, R.; Mari, C. M.; Cui, Y.; Kim, D. K. *Nano Letters* **2010,** 10, (10), 3852-3856.
42. Ding, Y. L.; Xie, J.; Cao, G. S.; Zhu, T. J.; Yu, H. M.; Zhao, X. B. *Advanced Functional Materials* **2011,** 21, (2), 348-355.
43. Jiao, F.; Bao, J.; Hill, A. H.; Bruce, P. G. *Angewandte Chemie* **2008,** 120, (50), 9857-9862.
44. Yuan, L.-X.; Wang, Z.-H.; Zhang, W.-X.; Hu, X.-L.; Chen, J.-T.; Huang, Y.-H.; Goodenough, J. B. *Energy & Environmental Science* **2011,** 4, (2), 269-284.
45. Wang, J.; Sun, X. *Energy & Environmental Science* **2012,** 5, (1), 5163-5185.
46. Prosini, P. P.; Lisi, M.; Zane, D.; Pasquali, M. *Solid State Ionics* **2002,** 148, (1), 45-51.
47. Zhang, W.-J. *Journal of Power Sources* **2011,** 196, (6), 2962-2970.
48. Fey, G. T.-K.; Chen, Y. G.; Kao, H.-M. *Journal of Power Sources* **2009,** 189, (1), 169-178.
49. Saravanan, K.; Balaya, P.; Reddy, M.; Chowdari, B.; Vittal, J. J. *Energy & Environmental Science* **2010,** 3, (4), 457-463.
50. Saravanan, K.; Reddy, M.; Balaya, P.; Gong, H.; Chowdari, B.; Vittal, J. J. *Journal of Materials Chemistry* **2009,** 19, (5), 605-610.
51. Kim, J.-K.; Manuel, J.; Lee, M.-H.; Scheers, J.; Lim, D.-H.; Johansson, P.; Ahn, J.-H.; Matic, A.; Jacobsson, P. *Journal of Materials Chemistry* **2012,** 22, (30), 15045-15049.
52. Wang, Y.; Feng, Z.-S.; Chen, J.-J.; Zhang, C. *Materials Letters* **2012,** 71, 54-56.
53. Herle, P. S.; Ellis, B.; Coombs, N.; Nazar, L. *Nature Materials* **2004,** 3, (3), 147-

152.
54. Liao, X.-Z.; He, Y.-S.; Ma, Z.-F.; Zhang, X.-M.; Wang, L. *Journal of Power Sources* **2007,** 174, (2), 720-725.
55. Padhi, A. K.; Nanjundaswamy, K.; Goodenough, J. *Journal of the Electrochemical Society* **1997,** 144, (4), 1188-1194.
56. Delacourt, C.; Laffont, L.; Bouchet, R.; Wurm, C.; Leriche, J.-B.; Morcrette, M.; Tarascon, J.-M.; Masquelier, C. *Journal of the Electrochemical Society* **2005,** 152, (5), A913-A921.
57. Meethong, N.; Huang, H.; Speakman, S. A.; Carter, W. C.; Chiang, Y. M. *Advanced Functional Materials* **2007,** 17, (7), 1115-1123.
58. Yonemura, M.; Yamada, A.; Takei, Y.; Sonoyama, N.; Kanno, R. *Journal of the Electrochemical Society* **2004,** 151, (9), A1352-A1356.
59. Palacin, M. R. *Chemical Society Reviews* **2009,** 38, (9), 2565-2575.
60. Dahn, J. R.; Zheng, T.; Liu, Y.; Xue, J. *Science* **1995,** 270, (5236), 590.
61. Novoselov, K.; Geim, A.; Morozov, S.; Jiang, D.; Zhang, Y.; Dubonos, S.; Grigorieva, I.; Firsov, A., Science **2004**, 306, (5696), 666.
62. Cui, L.-F.; Yang, Y.; Hsu, C.-M.; Cui, Y. *Nano letters* **2009,** 9, (9), 3370-3374.
63. Derrien, G.; Hassoun, J.; Panero, S.; Scrosati, B. *Advanced Materials* **2007,** 19, (17), 2336-2340.
64. Park, C.-M.; Kim, J.-H.; Kim, H.; Sohn, H.-J. *Chemical Society Reviews* **2010,** 39, (8), 3115-3141.
65. Wu, H.; Cui, Y. *Nano Today* **2012,** 7, (5), 414-429.
66. Yao, Y.; Liu, N.; McDowell, M. T.; Pasta, M.; Cui, Y. *Energy & Environmental Science* **2012,** 5, (7), 7927-7930.
67. Lee, J. K.; Smith, K. B.; Hayner, C. M.; Kung, H. H. *Chemical Communications* **2010,** 46, (12), 2025-2027.
68. McDowell, M. T.; Lee, S. W.; Ryu, I.; Wu, H.; Nix, W. D.; Choi, J. W.; Cui, Y. *Nano Letters* **2011,** 11, (9), 4018-4025.
69. Liu, N.; Wu, H.; McDowell, M. T.; Yao, Y.; Wang, C.; Cui, Y. *Nano Letters* **2012,** 12, (6), 3315-3321.
70. Yu, S. H.; Lee, S. H.; Lee, D. J.; Sung, Y. E.; Hyeon, T. *Small* **2016** , 12, (16), 2146–2172.
71. Lee, S. H.; Yu, S.-H.; Lee, J. E.; Jin, A.; Lee, D. J.; Lee, N.; Jo, H.; Shin, K.; Ahn, T.-Y.; Kim, Y.-W. *Nano Letters* **2013,** 13, (9), 4249-4256.
72. Lee, J. E.; Yu, S.-H.; Lee, D. J.; Lee, D.-C.; Han, S. I.; Sung, Y.-E.; Hyeon, T. *Energy & Environmental Science* **2012,** 5, (11), 9528-9533.
73. Lowe, M. A.; Gao, J.; Abruña, H. D. *Journal of Materials Chemistry A* **2013,** 1, (6), 2094-2103.
74. Jiang, H.; Hu, Y.; Guo, S.; Yan, C.; Lee, P. S.; Li, C. *ACS Nano* **2014,** 8, (6), 6038-6046.
75. Wang, H.; Cui, L.-F.; Yang, Y.; Sanchez Casalongue, H.; Robinson, J. T.; Liang, Y.; Cui, Y.; Dai, H. *Journal of the American Chemical Society* **2010,** 132, (40), 13978-13980.
76. Sun, H.; Xin, G.; Hu, T.; Yu, M.; Shao, D.; Sun, X.; Lian, J. *Nature Communications* **2013,** 5, 4526-4526.
77. Huang, X. l.; Wang, R. z.; Xu, D.; Wang, Z. l.; Wang, H. g.; Xu, J. j.; Wu, Z.; Liu, Q. c.; Zhang, Y.; Zhang, X. b. *Advanced Functional Materials* **2013,** 23, (35), 4345-4353.

78. Xie, X.; Ao, Z.; Su, D.; Zhang, J.; Wang, G. *Advanced Functional Materials* **2015,** 25, (9), 1393-1403.
79. Kim, T.-J.; Kim, C.; Son, D.; Choi, M.; Park, B. *Journal of Power Sources* **2007,** 167, (2), 529-535.
80. Vaughn, D. D.; Hentz, O. D.; Chen, S.; Wang, D.; Schaak, R. E. *Chemical Communications* **2012,** 48, (45), 5608-5610.
81. Todd, A.; Ferguson, P.; Fleischauer, M.; Dahn, J. *International Journal of Energy Research* **2010,** 34, (6), 535-555.
82. Deng, D.; Lee, J. Y. *Angewandte Chemie International Edition* **2009,** 48, (9), 1660-1663.
83. Zhang, N.; Zhao, Q.; Han, X.; Yang, J.; Chen, J. *Nanoscale* **2014,** 6, (5), 2827-2832.
84. Zhang, B.; Huang, J. Q.; Kim, J. K. *Advanced Functional Materials* **2015,** 25, (32), 5222-5228.
85. Qin, J.; He, C.; Zhao, N.; Wang, Z.; Shi, C.; Liu, E.-Z.; Li, J. *ACS Nano* **2014,** 8, (2), 1728-1738.
86. Zou, Y.; Wang, Y. *ACS Nano* **2011,** 5, (10), 8108-8114.
87. Xu, K. *Chemical Reviews* **2004,** 104, (10), 4303-4418.
88. Kalhoff, J.; Eshetu, G. G.; Bresser, D.; Passerini, S. *ChemSusChem* **2015,** 8, (13), 2154-2175.
89. Tan, S.; Ji, Y. J.; Zhang, Z. R.; Yang, Y. *ChemPhysChem* **2014,** 15, (10), 1956-1969.
90. Arai, J.; Katayama, H.; Akahoshi, H. *Journal of the Electrochemical Society* **2002,** 149, (2), A217-A226.
91. Kalhoff, J.; Bresser, D.; Bolloli, M.; Alloin, F.; Sanchez, J. Y.; Passerini, S. *ChemSusChem* **2014,** 7, (10), 2939-2946.
92. Tarascon, J.; Guyomard, D. *Solid State Ionics* **1994,** 69, (3-4), 293-305.
93. Ue, M.; Mori, S. *Journal of The Electrochemical Society* **1995,** 142, (8), 2577-2581.
94. Marom, R.; Haik, O.; Aurbach, D.; Halalay, I. C. *Journal of the Electrochemical Society* **2010,** 157, (8), A972-A983.
95. Newman, G.; Francis, R.; Gaines, L.; Rao, B. *Journal of The Electrochemical Society* **1980,** 127, (9), 2025-2027.
96. Beaulieu, L.; Eberman, K.; Turner, R.; Krause, L.; Dahn, J. *Electrochemical and Solid-State Letters* **2001,** 4, (9), A137-A140.
97. Key, B.; Bhattacharyya, R.; Morcrette, M.; Seznec, V.; Tarascon, J.-M.; Grey, C. P. *Journal of the American Chemical Society* **2009,** 131, (26), 9239-9249.
98. Wang, L.; Dong, Z.; Wang, D.; Zhang, F.; Jin, J. *Nano Letters* **2013,** 13, (12), 6244-6250.
99. Kovalenko, I.; Zdyrko, B.; Magasinski, A.; Hertzberg, B.; Milicev, Z.; Burtovyy, R.; Luzinov, I.; Yushin, G. *Science* **2011,** 334, (6052), 75-79.
100. Koo, B.; Kim, H.; Cho, Y.; Lee, K. T.; Choi, N. S.; Cho, J. *Angewandte Chemie International Edition* **2012,** 51, (35), 8762-8767.
101. Ling, M.; Zhao, H.; Xiao, X.; Shi, F.; Wu, M.; Qiu, J.; Li, S.; Song, X.; Liu, G.; Zhang, S. *Journal of Materials Chemistry A* **2015,** 3, (5), 2036-2042.
102. Yabuuchi, N.; Kubota, K.; Dahbi, M.; Komaba, S. *Chemical Reviews* **2014,** 114, (23), 11636-11682.
103. Tarascon, J. M.; Armand, M. *Nature* **2001,** 414, (6861), 359-367.

104. Goodenough, J. B.; Kim, Y. *Chemistry of Materials* **2010,** 22, (3), 587-603.
105. Obrovac, M. N.; Chevrier, V. L. *Chemical Reviews* **2014,** 114, (23), 11444-11502.
106. Dunn, B.; Kamath, H.; Tarascon, J. M. *Science* **2011,** 334, (6058), 928-935.
107. Whittingham, M. S. *Chemical Reviews* **2004,** 104, (10), 4271-4302.
108. Deng, D.; Kim, M. G.; Lee, J. Y.; Cho, J. *Energy & Environmental Science* **2009,** 2, (8), 818-837.
109. Aravindan, V.; Lee, Y. S.; Madhavi, S. *Advanced Energy Materials* **2015,** 5, (13).
110. Kim, M. G.; Sim, S.; Cho, J. *Advanced Materials* **2010,** 22, (45), 5154-5158.
111. Wang, Y.-X.; Huang, L.; Chang, Y.-Q.; Ke, F.-S.; Li, J.-T.; Sun, S.-G. *Electrochemistry Communications* **2010,** 12, (9), 1226-1229.
112. Xue, L.-J.; Xu, Y.-F.; Huang, L.; Ke, F.-S.; He, Y.; Wang, Y.-X.; Wei, G.-Z.; Li, J.-T.; Sun, S.-G. *Electrochimica Acta* **2011,** 56, (17), 5979-5987.
113. Derrien, G.; Hassoun, J.; Panero, S.; Scrosati, B. *Advanced Materials* **2007,** 19, (17), 2336-2340.
114. Xu, Y.; Liu, Q.; Zhu, Y.; Liu, Y.; Langrock, A.; Zachariah, M. R.; Wang, C. *Nano letters* **2013,** 13, (2), 470-474.
115. Zhu, Z.; Wang, S.; Du, J.; Jin, Q.; Zhang, T.; Cheng, F.; Chen, J. *Nano Letters* **2013,** 14, (1), 153-157.
116. Wang, Y.; Wu, M.; Jiao, Z.; Lee, J. Y. *Chemistry of Materials* **2009,** 21, (14), 3210-3215.
117. Kumar, T. P.; Ramesh, R.; Lin, Y.; Fey, G. T.-K. *Electrochemistry Communications* **2004,** 6, (6), 520-525.
118. Li, X.; Dhanabalan, A.; Gu, L.; Wang, C. *Advanced Energy Materials* **2012,** 2, (2), 238-244.
119. Qin, J.; He, C.; Zhao, N.; Wang, Z.; Shi, C.; Liu, E.-Z.; Li, J. *ACS Nano* **2014,** 8, (2), 1728-1738.
120. Wang, L.; Dong, Z.; Wang, D.; Zhang, F.; Jin, J. *Nano Letters* **2013,** 13, (12), 6244-6250.
121. Kovalenko, I.; Zdyrko, B.; Magasinski, A.; Hertzberg, B.; Milicev, Z.; Burtovyy, R.; Luzinov, I.; Yushin, G. *Science* **2011,** 334, (6052), 75-79.
122. Koo, B.; Kim, H.; Cho, Y.; Lee, K. T.; Choi, N. S.; Cho, J. *Angewandte Chemie. International Edition* **2012,** 51, (35), 8762-8767.
123. Ling, M.; Zhao, H.; Xiaoc, X.; Shi, F.; Wu, M.; Qiu, J.; Li, S.; Song, X.; Liu, G.; Zhang, S. *Journal of Materials Chemistry A* **2015,** 3, (5), 2036-2042.
124. Nikolic, G.; Zlatkovic, S.; Cakic, M.; Cakic, S.; Lacnjevac, C.; Rajic, Z. *Sensors* **2010,** 10, (1), 684-696.
125. Hassan, F. M.; Chen, Z.; Yu, A.; Chen, Z.; Xiao, X. *Electrochimica Acta* **2013,** 87, 844-852.
126. Wen, Z.; Cui, S.; Kim, H.; Mao, S.; Yu, K.; Lu, G.; Pu, H.; Mao, O.; Chen, J. *Journal of Materials Chemistry* **2012,** 22, (8), 3300-3306.
127. Guo, Z.; Zhao, Z.; Liu, H.; Dou, S. *Carbon* **2005,** 43, (7), 1392-1399.
128. Beaulieu, L. Y.; Eberman, K. W.; Turner, R. L.; Krause, L. J.; Dahn, J. R. *Electrochemical and Solid State Letters* **2001,** 4, (9), A137-A140.
129. Bridel, J.-S.; Azais, T.; Morcrette, M.; Tarascon, J.-M.; Larcher, D. *Chemistry of Materials* **2009,** 22, (3), 1229-1241.
130. Liu, C.-j.; Huang, H.; Cao, G.-z.; Xue, F.-h.; Camacho, R. A. P.; Dong, X.-l.

Electrochimica Acta **2014,** 144, 376-382.
131. Lee, D.-H.; Shim, H.-W.; Kim, J.-C.; Kim, D.-W. *Rsc Advances* **2014,** 4, (84), 44563-44567.
132. Dunn, B.; Kamath, H.; Tarascon, J.-M. *Science* **2011,** 334, (6058), 928-935.
133. Ogasawara, T.; Débart, A.; Holzapfel, M.; Novák, P.; Bruce, P. G. *Journal of the American Chemical Society* **2006,** 128, (4), 1390-1393.
134. Girishkumar, G.; McCloskey, B.; Luntz, A.; Swanson, S.; Wilcke, W. *The Journal of Physical Chemistry Letters* **2010,** 1, (14), 2193-2203.
135. Bruce, P. G.; Freunberger, S. A.; Hardwick, L. J.; Tarascon, J.-M. *Nature materials* **2012,** 11, (1), 19-29.
136. Ji, X.; Lee, K. T.; Nazar, L. F. *Nature materials* **2009,** 8, (6), 500-506.
137. Yabuuchi, N.; Kubota, K.; Dahbi, M.; Komaba, S. *Chemical reviews* **2014,** 114, (23), 11636-11682.
138. Xin, S.; Yin, Y. X.; Guo, Y. G.; Wan, L. J. *Advanced Materials* **2014,** 26, (8), 1261-1265.
139. Kim, S. W.; Seo, D. H.; Ma, X.; Ceder, G.; Kang, K. *Advanced Energy Materials* **2012,** 2, (7), 710-721.
140. Weber, A. Z.; Mench, M. M.; Meyers, J. P.; Ross, P. N.; Gostick, J. T.; Liu, Q. *Journal of Applied Electrochemistry* **2011,** 41, (10), 1137-1164.
141. Ulaganathan, M.; Aravindan, V.; Yan, Q.; Madhavi, S.; Skyllas‐Kazacos, M.; Lim, T. M. *Advanced Materials Interfaces* **2016,** 3, (1).
142. Etacheri, V.; Marom, R.; Elazari, R.; Salitra, G.; Aurbach, D. *Energy & Environmental Science* **2011,** 4, (9), 3243-3262.
143. Tarascon, J.-M.; Armand, M. *Nature* **2001,** 414, (6861), 359-367.
144. Winter, M.; Besenhard, J. O. *Electrochimica Acta* **1999,** 45, (1), 31-50.
145. Zhou, X.; Wan, L. J.; Guo, Y. G. *Advanced Materials* **2013,** 25, (15), 2152-2157.
146. Xu, Y.; Liu, Q.; Zhu, Y.; Liu, Y.; Langrock, A.; Zachariah, M. R.; Wang, C. *Nano Letters* **2013,** 13, (2), 470-474.
147. Kravchyk, K.; Protesescu, L.; Bodnarchuk, M. I.; Krumeich, F.; Yarema, M.; Walter, M.; Guntlin, C.; Kovalenko, M. V. *Journal of the American Chemical Society* **2013,** 135, (11), 4199-4202.
148. Wang, L.; Wang, D.; Dong, Z.; Zhang, F.; Jin, J. *Nano Letters* **2013,** 13, (4), 1711-1716.
149. Chen, J. S.; Lou, X. W. D. *small* **2013,** 9, (11), 1877-1893.
150. Jahel, A.; Ghimbeu, C. M.; Monconduit, L.; Vix‐Guterl, C. *Advanced Energy Materials* **2014,** 4, (11).
151. Qin, J.; He, C.; Zhao, N.; Wang, Z.; Shi, C.; Liu, E.-Z.; Li, J. *ACS Nano* **2014,** 8, (2), 1728-1738.
152. Li, X.; Dhanabalan, A.; Gu, L.; Wang, C. *Advanced Energy Materials* **2012,** 2, (2), 238-244.
153. Zhu, Z.; Wang, S.; Du, J.; Jin, Q.; Zhang, T.; Cheng, F.; Chen, J. *Nano Letters* **2013,** 14, (1), 153-157.
154. Wolfenstine, J.; Allen, J. L.; Read, J.; Foster, D. *Chemistry and Structure of Sony's Nexelion Li-ion Electrode Materials*; DTIC Document: 2006.
155. Wang, Y.; Wu, M.; Jiao, Z.; Lee, J. Y. *Chemistry of Materials* **2009,** 21, (14), 3210-3215.
156. Zhang, H. X.; Feng, C.; Zhai, Y. C.; Jiang, K. L.; Li, Q. Q.; Fan, S. S. *Advanced*

Materials **2009,** 21, (22), 2299-2304.
157. Wen, Z.; Wang, Q.; Zhang, Q.; Li, J. *Advanced Functional Materials* **2007,** 17, (15), 2772-2778.
158. Chen, B.; Qian, H.; Xu, J.; Qin, L.; Wu, Q.-H.; Zheng, M.; Dong, Q. *Journal of Materials Chemistry A* **2014,** 2, (24), 9345-9352.
159. Wen, Z.; Cui, S.; Kim, H.; Mao, S.; Yu, K.; Lu, G.; Pu, H.; Mao, O.; Chen, J. *Journal of Materials Chemistry* **2012,** 22, (8), 3300-3306.
160. Beck, F. R.; Epur, R.; Hong, D.; Manivannan, A.; Kumta, P. N. *Electrochimica Acta* **2014,** 127, 299-306.
161. Wang, G.; Wang, B.; Wang, X.; Park, J.; Dou, S.; Ahn, H.; Kim, K. *Journal of Materials Chemistry* **2009,** 19, (44), 8378-8384.
162. Paek, S.-M.; Yoo, E.; Honma, I. *Nano Letters* **2008,** 9, (1), 72-75.
163. Dhanabalan, A.; Li, X.; Agrawal, R.; Chen, C.; Wang, C. *Nanomaterials* **2013,** 3, (4), 606-614.
164. Jiang, Y.; Yuan, T.; Sun, W.; Yan, M. *ACS Applied Materials & Interfaces* **2012,** 4, (11), 6216-6220.
165. Park, S.-K.; Yu, S.-H.; Pinna, N.; Woo, S.; Jang, B.; Chung, Y.-H.; Cho, Y.-H.; Sung, Y.-E.; Piao, Y. *Journal of Materials Chemistry* **2012,** 22, (6), 2520-2525.
166. Zhang, L.; Wu, H. B.; Lou, X. D. W. *Materials Horizons* **2014,** 1, (1), 133-138.
167. Chen, S.; Wang, Y.; Ahn, H.; Wang, G. *Journal of Power Sources* **2012,** 216, 22-27.
168. Larcher, D.; Beattie, S.; Morcrette, M.; Edstroem, K.; Jumas, J.-C.; Tarascon, J.-M. *Journal of Materials Chemistry* **2007,** 17, (36), 3759-3772.
169. Liu, H. K.; Wang, G. X.; Guo, Z.; Wang, J.; Konstantinov, K. *Journal of Nanoscience and Nanotechnology* **2006,** 6, (1), 1-15.
170. Dieguez, A.; Romano-Rodrıguez, A.; Vila, A.; Morante, J. *Journal of Applied Physics* **2001,** 90, (3), 1550-1557.
171. Dresselhaus, M. S.; Jorio, A.; Hofmann, M.; Dresselhaus, G.; Saito, R. *Nano Letters* **2010,** 10, (3), 751-758.
172. Liang, J.; Yu, X. Y.; Zhou, H.; Wu, H. B.; Ding, S.; Lou, X. W. D. *Angewandte Chemie. International Edition* **2014,** 53, (47), 12803-12807.

LIST OF PUBLICATIONS

(1) **Y. F. Xu**, Y.-X. Wang, J.P. Yang, W. Lai, S.-L. Chou, D. Wexler; Oleic acid derived facile self-growth approach to graphene-confined Sn@SnO_2 nanocomposites for high lithium storage capacity; manuscript under processing.

(2) Y.-X. Wang, **Y. F. Xu**, Q.-S. Meng, S.-L. Chou, J. Ma, H. K. Liu; Chemically bonded tin nanoparticles with epoxy binder for high-performance lithium ion batteries; *Advanced Materials Interfaces*, 2016, 23, 1600662.

(3) J. P. Yang, Y.-X. Wang, S.-L. Chou, R. Y. Zhang, **Y. F. Xu**, J. Fan, W. Zhang, H. K. Liu, D. Zhao, S. X. Dou; Yolk-shell silicon-mesoporous carbon anode with compact solid electrolyte interphase film for superior lithium-ion batteries; *Nano Energy*, 2015, 18, 133.

(4) B. Ruan, J. Wang, D. Shi, **Y. F. Xu**, S. Chou, H. Liu, J. Wang; A phosphorus/N-doped carbon nanofiber composite as an anode material for sodium-ion batteries; *J. Mater. Chem. A,* 2015, 3, 19011.

(5) W. Luo, Y.-X. Wang, S.-L. Chou, **Y. F. Xu** , W. Li, B. Kong, S. X. Dou, H. K. Liu, J.P. Yang; Critical thickness of phenolic resin-based carbon interfacial layer for improving long cycling stability of silicon nanoparticle anodes; *Nano Energy*, 2016, 27, 255.